Modelling Photocatalytic N₂ Reduction to Ammonia: Where We Stand and Where We Are Going

Taja Žibert,[a, b] Blaž Likozar,*[a] and Matej Huš*[a, b, c, d]

Artificial ammonia synthesis via the Haber-Bosch process is environmentally problematic due to the high energy consumption and corresponding CO₂ emissions, produced during the reaction and before hand in hydrogen production upon methane steam reforming. Photocatalytic nitrogen fixation as a greener alternative to the conventional Haber-Bosch process enables us to perform nitrogen reduction reaction (NRR) under mild conditions, harnessing light as the energy source. Herein, we systematically review first-principles calculations used to determine the electronic/optical properties of photocatalysts, N₂ adsorption and to expound possible NRR mechanisms. The most commonly studied photocatalysts for nitrogen fixation are usually modified with dopants, defects, co-catalysts and Z-scheme heterojunctions to prevent charge carrier recombination, improve charge separation efficiency and adjust a band gap to for utilizing a broader light spectrum. Most studies at the atomistic level of modeling are grounded upon density functional theory (DFT) calculations, wholly foregoing excitation effects paramount in photocatalysis. Hence, there is a dire need to consider methods beyond DFT to study the excited state properties more accurately. Furthermore, a few studies have been examined, which include higher level kinetics and macro-scale simulations. Ultimately, we show there is still ample room for improvement with regard to first principles calculations and their integration in multiscale models.

1. Introduction

Nitrogen is one of the most abundant elements in the Earth's atmosphere (78%), and nitrogen-containing compounds are essential for a variety of different biochemical processes and build several compounds such as amino acids, nucleic acids, and proteins.[1] Nitrogen is also involved in the nitrogen cycle of plants.[2] Biological nitrogen fixation is carried out by an enzyme nitrogenase, which most plants and animals do not have[1,3,4] and instead rely on microorganisms.

Synthetic ammonia is used as a fertilizer, explosive,[5,6] chemical,[5,7] energy[5] and chemical hydrogen (hydrogen density up to 17%[7,8]). The Haber-Bosch process is still the leading process of industrial ammonia synthesis, but its poor environmental impact has prompted scientists to search for environmentally friendlier methods.[1,4,9,10] Hydrogen as its feedstock is typically produced from methane by steam reforming ($CH_4 + 2H_2O \rightarrow 4H_2 + CO_2$), causing significant CO₂ emissions (∼1.2%).[1,3,5,11] High energy input is also needed to break a strong triple bond in the nitrogen molecule (941 kJmol⁻¹), requiring high temperatures (up to 500°C) and pressures (200 atm).[4,10]

Photocatalysis on the other hand uses water as a viable proton source and light as the driving force.[1,12] In 1977, Schrauzer and Guth reported the first photocatalytic fixation of nitrogen, having performed photocatalytic nitrogen reduction over a TiO₂ based photocatalyst and detected ammonia as the main product.[13] Ever since, numerous photocatalysts have been explored for this reaction. The most promising groups entail metal oxides, bismuth oxyhalides, carbonaceous materials, metal sulfides, and bio-mimicking photocatalysts.[4]

While a major advantage of photocatalytic reactions is the use of sustainable energy sources,[4,12] finding an efficient photocatalyst is hard. Pristine photocatalysts are usually plagued with low yields and require UV light due to their wide band gaps.[3,4] Thus, it is common to modify their structure with dopants, defects, co-catalysts, or heterojunctions.[1,4,14] For intelligent catalyst design and reaction understanding, modelling is becoming indispensable.

This review aims to describe first-principles based multiscale modelling of the photocatalytic NRR. Section 2 presents the theoretical fundamentals, including photoexcitations, adsorption, reaction mechanisms, and catalyst modifications. The theoretical methods within a multiscale modeling approach in Section 3 are followed by the overview of the calculated electronic properties in Section 4, kinetic modelling in section 5 and reactor modeling in section 6. Lastly, the findings and future prospects are presented.

[a] T. Žibert, B. Likozar, M. Huš
National Institute of Chemistry, Department of Catalysis and Chemical
Reaction Engineering, Hajdrihova 19, SI-1001 Ljubljana, Slovenia
E-mail: blaz.likozar@ki.si
           matej.hus@ki.si

[b] T. Žibert, M. Huš
University of Nova Gorica, Vipavska 13, 5000 Nova Gorica, Slovenia

[c] M. Huš
Institute for the Protection of Cultural Heritage, Poljanska 40,
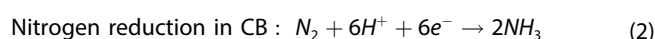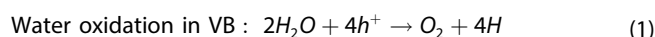SI-1000 Ljubljana, Slovenia

[d] M. Huš
Association for Technical Culture (ZOTKS), Zaloška 65,
SI-1001 Ljubljana, Slovenia

2. Fundamentals of Nitrogen Photofixation

Nitrogen is an inert molecule with a high ionization potential of 15 eV, a negative electron affinity of −1.8 eV, a large energy band gap of 22.9 eV, and a bond dissociation energy of 941 kJmol⁻¹. Therefore, its activation remains challenging.[3,4] NRR is thermocatalytically performed under harsh conditions despite being exothermic with an enthalpy change (ΔH (298 K)) of −92.2 kJ/mol.[15]

Its photoreduction requires six electrons and protons to convert one N_2 into two ammonia molecules. Along with the oxidation of water, the corresponding reduction potentials are displayed in Eqs. 1 and 2, respectively, and shown in Figure 1:[4,14]

$$\text{Water oxidation in VB}: \quad 2H_2O + 4h^+ \rightarrow O_2 + 4H \tag{1}$$

$$\text{Nitrogen reduction in CB}: \quad N_2 + 6H^+ + 6e^- \rightarrow 2NH_3 \tag{2}$$

The reduction potentials of NRR vs a normal hydrogen electrode (NHE) at pH 0 are shown in Table 1. In the nitrogen reduction reaction, first bond cleavage requires a reduction potential of −4.2 V vs. NHE, indicating that first bond cleavage in nitrogen is challenging for most semiconductors.[3] It is important to remember that the selectivity of photocatalytic nitrogen reduction is limited by competing hydrogen evolution reaction (HER), oxygen reduction reaction (ORR), and also oxygen evolution reaction (OER).[16] Since the reaction potentials of NRR and HER are very similar, HER competes with NRR and impairs its selectivity. To mitigate HER, the photocatalyst and operating conditions for NRR must be controlled and chosen wisely.[17,18]

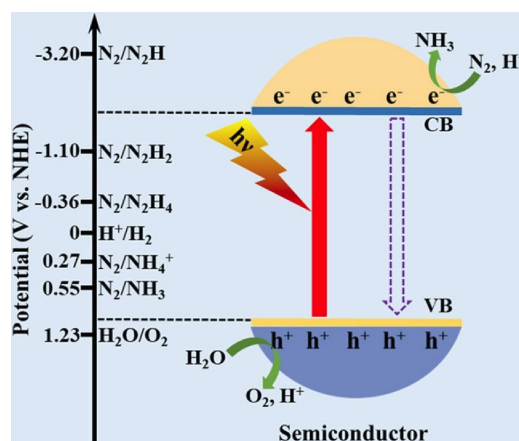Upon irradiation, electrons are ejected from from the valence band (VB) to the conduction band (CB), leaving a hole.

Figure 1. Schematic representation of a semiconductor photocatalyst showing reduction potentials for nitrogen reduction and water oxidation reactions. Potentials are presented at pH 0. Reprinted with permission from [15].

Table 1. Reduction potentials of NRR at pH 0.[3]

Reaction	Potential vs NHE [V]
$N_2 + e^- \rightarrow N_2^-$ (aq)	−4.20
$N_2 + H^+ + e^- \rightarrow N_2H$	−3.20
$N_2 + 2H^+ + 2e^- \rightarrow N_2H_2$	−1.10
$N_2 + 4H^+ + 4e^- \rightarrow N_2H_4$	−0.36
$N_2 + 5H^+ + 4e^- \rightarrow N_2H_5^+$	−0.23
$N_2 + 6H^+ + 6e^- \rightarrow 2NH_3$	+0.55
$N_2 + 8H^+ + 8e^- \rightarrow 2N_2H_4^+$	+0.27

The photogenerated electrons and holes must migrate to the active sites of the photocatalyst for the reaction to proceed.
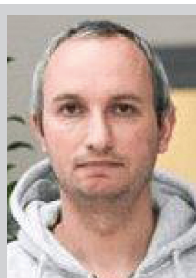
Prof. Blaž Likozar is the head of the Department of Catalysis and Chemical Reaction Engineering at the National Institute of Chemistry (Ljubljana, Slovenia). He leads numerous research projects, including 15 in H2020/30 in Horizon Europe, and is involved in several industrial projects. His areas of expertise include heterogeneous catalysis, chemical kinetics, transport phenomena, simulations and modelling, and optimization of process fluid mechanics. He has authored over 300 articles, has been cited over 800 times and has an h-index of 45.

Dr Matej Huš is a senior researcher at the National Institute of Chemistry (Ljubljana, Slovenia) and a lecturer at the University of Nova Gorica. His field of expertise is computational chemistry, with an emphasis on nitrogen fixation, carbon dioxide hydrogenation, methane activation, ethylene epoxidation, and biomass valorization. His research covers all types of catalysis.

Taja Žibert is a PhD student at the Department of Catalysis and Chemical Reaction Engineering, National Institute of Chemistry (Ljubljana, Slovenia). Her research focuses on first-principles based multi-scale modelling of photocatalytic nitrogen reduction reaction over titanium dioxide clusters.

ChemSusChem

Review
doi.org/10.1002/cssc.202301730

Chemistry Europe
European Chemical
Societies Publishing

Since their recombination depresses the photocatalytic activity, it is hindered by using metals as dopants and electron trappers. When the electron is excited from the valence band, the metal traps it on the active site, where the photooxidation and photoreduction reactions occur. The holes react with water in the conduction band.

When considering photocatalytic reactions, some features should be taken into consideration. The positions of the band edges and the width of the band gap determine the wavelength (or energy) of the suitable light source. The energy of the band gap must match the photon energy (wavelength, λ) of the light source to excite the electrons ($\lambda = \frac{hc}{E}$, where h denotes the Planck constant, c the speed of light, and E the energy of the band gap). However, excessively narrow band gaps lead to the recombination of electron-hole pairs.[3,4,8,14] Photocatalytic activity depends mainly on the effectiveness of light utilization, electron-hole recombination, and the ability of electron-hole pairs to migrate to the active sites of photocatalysts.[19]

2.1. Reaction Mechanisms

Nitrogen reduction can occur through different pathways. In the dissociative pathway, the triple bond in N_2 is cleaved first, followed by successive hydrogenation, requiring a high initial energy input and making it less common in photocatalysis. Hydrogen is usually provided from the water molecule, which is oxidized in the valence band of the photocatalyst, while the protons and electrons from the conduction band of the photocatalyst react with nitrogen.[4,14]

The associative mechanism is reported to be more common with three possible pathways proposed: distal, alternating and enzymatic. In the alternating and distal pathway, the nitrogen molecule is adsorbed on the surface perpendicularly. It refers to the end-on configuration of the nitrogen molecule, which is typical for associative mechanisms as illustrated in Figure 2.

In the alternating pathway, the successive hydrogenation steps occur alternately at both nitrogen atoms, whereas in the distal pathway, they occur at the distal nitrogen atom until the first ammonia molecule is formed and desorbed. In the associative enzymatic mechanism both nitrogen atoms are adsorbed simultaneously on the catalyst surface and the triple bond is during the adsorption not broken (side-on configuration). Hydrogenation then occurs on both nitrogen atoms successively until two ammonia molecules are formed, desorbed and released from the surface.[3,4,15] The final desorption from the surface must happen at a relatively fast rate.[4]

2.2. Modifications in Photocatalysis

Photocatalytic reactions struggle with low product selectivity and poor quantum yields. This is an additional incentive to improve the photocatalyst properties and thus the photocatalytic activity and selectivity by modifying the catalyst
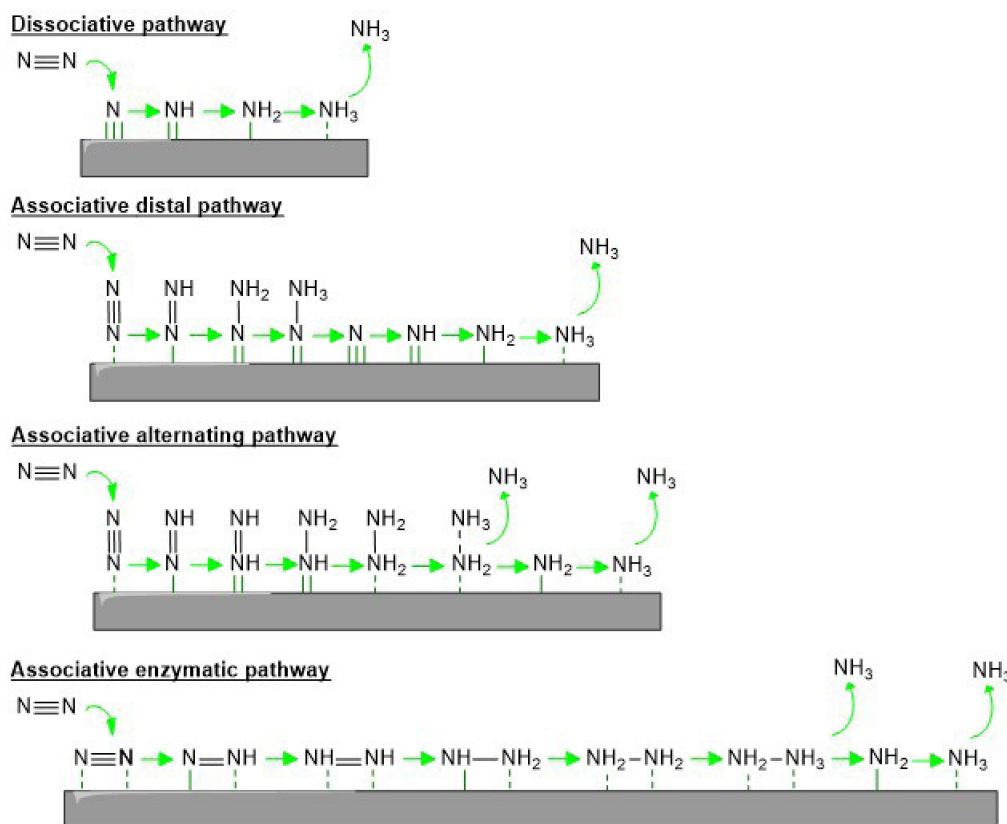

Figure 2. Dissociative, associative distal, associative alternating, and associative enzymatic pathways for nitrogen reduction process.

structure. Introduced defects, such as vacancies, or doping with heteroatoms act as electron trapping centers and therefore prevent electron-hole recombination and thus improve the photocatalytic properties. The most common modifications are defects, doping, co-catalysts, heterojunctions, strain and non-crystallinity.[1,4,14]

2.2.1. Defects

Anion vacancy defects, especially oxygen vacancies (OV) in transition metal oxides, play a crucial role. After their formation, the electron-rich environment is considered an electron trapping site that enables nitrogen adsorption by preventing charge carrier recombination. The electrons are transferred from the trapped OVs to the π anti-bonding orbital of the adsorbed nitrogen molecule, which is then activated. Low-valent cations near the OV facilitate the process. Similarly, sulfur and nitrogen vacancy formation can be explained. Metal sulfides are excellent photocatalysts due to good conductivity, fast and effective charge transfer and variable band gap. The formation of sulfur vacancies is not dependent on the size and morphology of the semiconductor particles, as is typical for other vacancy-rich photocatalysts. A decrease in particle size usually leads to an increased occurrence of anion vacancy defects.[1,20,21] On the other hand, nitrogen vacancies serve as promising active sites for nitrogen reduction because the size and shape of the vacancy corresponds to the size and shape of the nitrogen atom in the nitrogen molecule.[4]

2.2.2. Doping

In addition to vacancy formation, doping heteroatoms into the bulk structure of semiconductor photocatalyst or loading them on the catalyst surface is also an attractive way to provide promising active sites and promote nitrogen photoreduction. Doped heteroatoms introduce additional midgap states that act as electron trapping sites and enhance charge carrier separation, thus preventing electron-hole recombination.

2.2.3. Co-Catalysts

Heteroatoms on the surface of a semiconductor serve as active sites for chemical adsorption of nitrogen and water. Electrons and holes, generated in the photocatalyst, are transferred to the co-catalyst, where nitrogen adsorption takes place.[1] For instance, studying electron transfer between N$_2$ and Ru on a SV-CoS/CN photocatalyst, Yuan et al.[22] showed that electrons were transferred from a CoS$_x$ in CoS/CN to the Ru atom and then further to the π antibonding orbital in N$_2$.

2.2.4. Heterojunctions

Photocatalytic activity can be improved by combining two different photocatalysts, i.e. creating a heterojunction photocatalyst. Low et al. reported three common types of heterojunctions, i.e. type-I, type-II and type-III (shown in Figure 3). They are distinguished by the position of the VBs and CBs of the semiconductors. For a detailed description of each type of heterojunction, the reader is referred to Figure 3 and
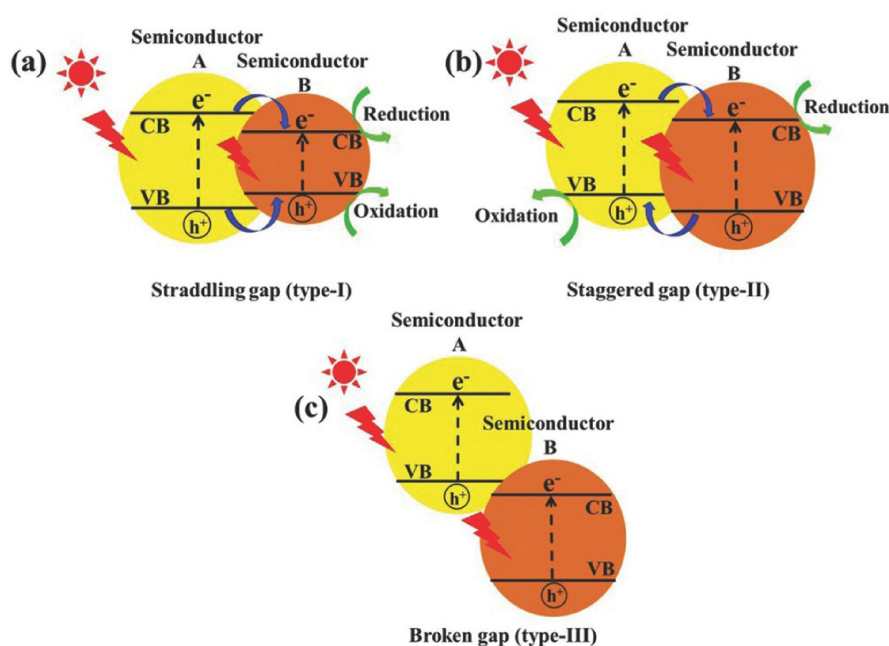

Figure 3. Three types of heterojunction semiconductors: a) type-I, b) type-II and c) type-III. Reprinted with permission from [23].

reference.[23,24] Among the three types, Z-scheme heterojunctions prevail in photocatalysis.

2.2.5. Strain and Non-Crystallinity

Strain and non-crystallinity also play important roles in defect engineering. The formation of OV causes a compressive strain in semiconductors, which stabilizes the OV and enhances N_2 activation. On the other hand, the additional amorphous surface structures help enhance the photocatalytic activity because the additional amorphous surface layer usually contains a high concentration of OVs as well as active sites localized on the amorphous surface.[1]

3. Theoretical Modelling

3.1. Multiscale Modelling

When a system of interest is studied at several scales (different length and time scales), one approach is not sufficient to describe all properties. In materials science and catalysis, calculations at the atomistic/quantum level are usually performed using DFT method because of its favourable cost/accuracy ration, which can be followed by an (*ab initio*) Molecular Dynamics simulations (AIMD) for elucidating dynamic properties. Kinetics can be studied using mean-field micro-kinetic modeling (MM) or kinetic Monte Carlo (kMC) methods, while reactor modeling is performed using a Computational Fluid Dynamics (CFD).[25–28] The multiscale modeling approach, integrating different levels of simulation,[27] is graphically presented in Figure 4.

3.2. Atomistic/Quantum Level

DFT is most commonly used to study the structure and properties of (photo)catalysts, yielding electronic, mechanical, magnetic, dielectric, and structural properties, crystal structures, phase diagrams, vibrational spectroscopy, surfaces, adsorption, electronic transport, and reaction mechanisms.[25,26] DFT rests upon the seminal work by Hohenberg and Kohn,[30] showing that all ground-state properties and thus total energy of a system depend on electron density (the Hohenberg-Kohn theorem[31,32]). Moreover, Kohn and Sham[33] reduced the many body problem of interacting particles (electrons) to an equivalent fictitous system of non-interacting electrons, introducing the exchange-correlation functional. However, this functional seems unknowable and several approximations have been devised to reflect the exchange-correlation part.[26,31–33]

In the local density approximation (LDA), local particle density is used, which is identical to the density of the homogeneous electron gas. Due to severe shortcomings of LDA (such as overestimating binding energies and underestimating band gaps), generalized-gradient approximation (GGA) was developed, which incorporates the gradient of the local density. GGA functionals perform better than LDA by significantly improving the atomization energies, cohesive energies and binding energies,[26] but they still cannot correctly predict the band gap due to the self-interaction error.[26,34] Approximations beyond LDA and GGA must be used to correctly predict the electronic properties[31] of semiconductors, which are crucial for photocatalysis. The meta-GGA approximation includes the Laplace operator, i.e. the second- order of the nabla operator to describe the kinetic energy.[26,35]

In contrast to LDA and GGA functionals, hybrid functionals are commonly used to predict the electronic properties since they contain a certain percentage of the Hartree-Fock exchange energy (from 20 to 100%, depending on the selected functional[36]). This makes hybrid functional empirical in the strict sense of the word. The hybrid exchange-correlation
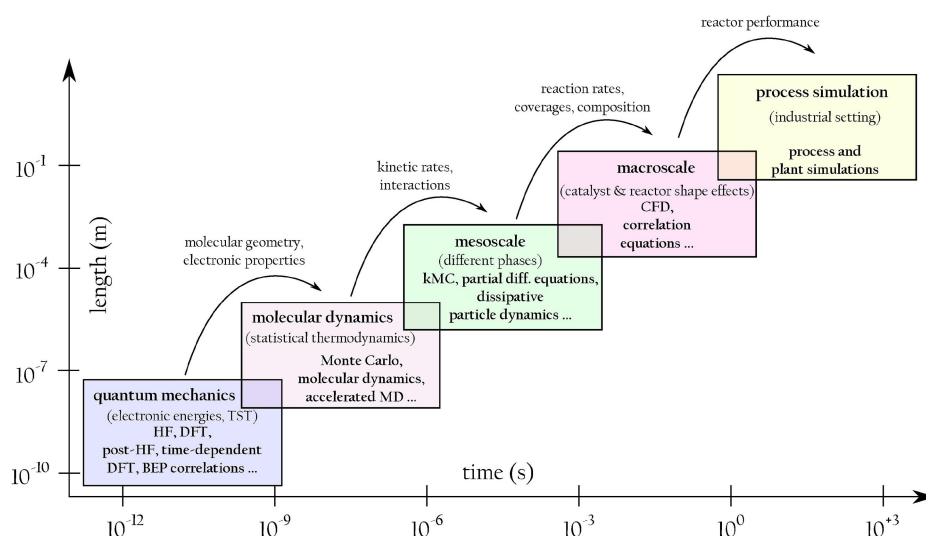

Figure 4. Multiscale model at different time and length scales. Reprinted with permission from [29].

ChemSusChem

Review
doi.org/10.1002/cssc.202301730

Chemistry
Europe
European Chemical
Societies Publishing

functionals, such as B3PW or B3LYP, allow to achieve an excellent agreement with experimentally obtained band gap values for the related complex oxide materials, whereas the GGA, or LDA exchange-correlation functionals usually underestimate them. The latter was nicely shown in determination of band gaps for various complex oxide materials, where the band gaps calculated with hybrid functionals, B3PW and B3LYP, showed an excellent agreement with experimentally determined values.[37,38] In an effort to eliminate the self-interaction error, one can use the GW method, which predicts the band gap more accurately but is computationally costly and cannot determine stresses and forces directly, limiting its use for studying the atomic structure.[26]

An important consideration is the inherent limitation of DFT, which describes ground state properties. To study the system under photocatalytic conditions, excited state calculations must be performed and therefore methods beyond DFT must be considered. At a comparable cost, excited state calculations can be performed using time-dependent density functional theory (TDDFT), Bethe-Salpeter equation (BSE), the delta self-consistent field method (ΔSCF) or the maximum overlap method (MOM). Higher level, multi-reference methods are usually too costly and do not work as out-of-the-box software packages.

Time-dependent DFT enables us to study excited-state properties in a linear-response or real-time regime. The latter allows for the determination of the linear absorption spectrum of excited system, a time-dependent dipole moment and a non-linear emission spectrum. The excitation energies and the photoelectron spectra (PES) are calculated in a linear-response regime.[39,40] The ΔSCF method is a density functional theory method, which enables the excitation of one or more electrons to higher energy states and thus a manual consideration of excited states. During the excitation process, an electron is excited from the valence band (or the highest occupied molecular orbital) into one of higher energy states.[41] This is problematic because the DFT-produced orbitals have no physical meaning. However, since the Kasha rule states that any excited-state reaction starts from the lowest excited state in the singlet or triplet state and is therefore independent of the excitation wavelength,[42] DFT methods are sometimes used to describe the lowest-lying excited state. On the other hand, the maximum overlap method (MOM) runs in the variational time-independent DFT framework, where the overlap between the occupied orbitals is maximized to prevent the system from collapsing to the ground state. A better and smoother convergence can be achieved by using a direct-optimization maximum overlap method (DO-MOM), which yields better results than the aforementioned SCF-MOM but is computationally more demanding.[43–45]

3.3. *Ab initio* Molecular Dynamics

Classical molecular dynamics (MD) simulations are based on solving the classical Newtonian equations of motion with the interatomic forces obtained from an empirical model or force fields. However, the forces can also be obtained from first-principles calculations (such as DFT or Hartree-Fock[27,28]), resulting in *ab initio* molecular dynamics simulations (AIMD). In AIMD simulations, the dynamic trajectories are generated at a finite temperature and the chemical bonds are allowed to break and form. As with all first-principles methods, it is paramount to choose an appropriate functional as it has a strong influence on the quality of the electronic structure. Thus, a total dipole moment and IR spectra can be calculated. In (photo)catalytic systems, AIMD is usually employed to confirm thermodynamic stability.[46–49]

3.4. Kinetic Modeling

DFT-derived data can be used to study the kinetics of heterogeneous reactions using mean-field microkinetic modeling (MKM) or kinetic Monte Carlo (kMC) simulations with an appropriate model, such as a gas model, a lattice model, and a reaction model. In the gas model, the mixture of gaseous reactants is represented at a defined temperature, pressure and mixture composition. In the lattice model, the catalyst surface is modeled and in the reaction model all possible reactions (surface processes) are predicted. Kinetic Monte Carlo is a stohastic method that can be used to describe different processes, such as adsorption, diffusion, reaction and desorption by solving the master equation.

In contrast to kMC, microkinetic modeling yields deterministic solutions by numerically solving the differential rate equations until the steady-state values converge and the turnover frequencies (TOF) are determined. Heat conduction, viscosity and diffusivity as examples of the transport processes that can be studied as well as reactions in the gas, liquid and gas-solid (surface) phases. After the reaction model is proposed, the kinetics of the given processes can be described and solved by the macroscopic rate equations, which include the rate coefficients related to the reaction rates. However, in the mean-field approximation the adsorbates are not correlated, leading to overestimating the catalytic activity.[50] In kMC, these correlations are taken into account, adding computational complexity.

3.5. Computational Fluid Dynamics

On a macro-scale, computational fluid dynamics (CFD) provides insight into reactor-related properties, i.e. the hydrodynamics of multiphases, light intensity distribution and reaction kinetics. It can model different reactor types, such as slurry photoreactor systems, where a (photo)catalyst is dispersed in the medium, and immobilized reactor systems, where the (photo)catalyst is deposited on the surface. In hydrodynamic modeling, the flow and the radiation fields are computed separately by solving the Navier-Stokes equations in a continuous limit for single phase systems or by using the Eulerian-Eulerian or Eulerian-Lagrangian models for multiphase flow systems. When considering the Eulerian-Eulerian model, the equations for solving the multi-

phase system represent the conservation of momentum and mass (and energy), while in the Eulerian-Lagrangian model the equation of motion is solved for dispersed phase particles and the continuous phase is considered by solving the Eulerian equations. When the concentration of the photocatalyst is relatively small the Eulerian-Lagrangian model is considered, while at higher concentrations the Eulerian-Eulerian model is predominant. Within the CFD framework, ensemble optical properties, such as the scattering coefficients, absorption coefficients, phase function parameter and optical parameters can be calculated.

3.6. Accounting for Illumination

When studying photocatalytic systems, the radiative transport equation (RTE) is employed to describe the light absorption of the illuminated light in the photoreactor as well as the out- and in-scattering irradiation. In slurry reactors, the RTE equation includes light absorption, in- and out-scattering. In immobilized systems (coated plates, monoliths, optical fibers), RTE equation can be reduced to the Beer-Lambert law upon negligible scattering effects. The RTE equation can be solved by considering analytical approximations or, more often, numerically with the Monte Carlo method, P1 model, discrete ordinate model (DO) or finite volume model (FV).[51,52]

3.7. Integrating/Coupling the Methods

Multi-scale models *by definition* involve coupling several levels of modelling: at least two. Outputs from a lower level simulation are used on a higher level, for instance DFT-computed reaction parameters in a kinetic model, which is further cast in a CFD simulation. In existing liteature, (photo)catalytic nitrogen reduction has been thoroughly studied over different pristine and modified photocatalysts in the ground state. Some DFT calculations were coupled with *ab initio* molecular dynamics to confirm the thermodynamic stability of the catalyst's structure or to observe the lifetime of charge carriers. Much less commonly, the atomistic calculations are integrated with microkinetic modelling or kinetic Monte Carlo to study the kinetics, whereas coupling with macro level simulations (computational fluid dynamics) is wholly missing. Furthermore, accounting for photoeffects (excited states) is usually neglected and is never used in multi-scale models.

4. First-Principles Calculations

4.1. Electronic Properties

As the knowledge of a catalyst structure and properties is paramount for studying the mechanism of nitrogen reduction, most studies incorporate at least rudimentary DFT calculations. They focus on the formation energies of catalyst defects, their band gap value, charge density difference, density of states and

projected density of states are investigated as the most straight-forward quantities to compute. Unfortunately, they are usually studied in the ground state, neglecting the excited states. Few studies include the investigation of the lifetime of charge carriers, which is simulated using molecular dynamics. Most DFT studies use still rely on GGA-based functionals (mostly PBE), at best supplemented by the Hubbard-U correction and the Grimme correction for van der Waals interactions. Using hybrid functionals is comparatively rarer. In the following sections, we group these studies according to the catalysts studied.

4.1.1. Pristine and Modified TiO_2 Photocatalysts

Band gaps and (projected) density of states are the most frequently studied electronic properties of pristine and modified TiO_2 photocatalysts, where oxygen vacancies are induced or different dopant atoms are doped into the pristine structure.[53–56] New states in the middle of the band gap (0.32 eV below the conduction band) were observed by Zhang et al.[54] who studied pristine anatase and OV-anatase TiO_2 (101) photocatalysts. Doping TiO_2 with Fe was investigated by Wu et al.[56] who introduced one positive charge to simulate a photogenerated hole and found that this charge is located at the Fe site (covered by polaron). Zhao et al.[53] calculated the band gap, density of states (DOS) and electron density diagrams of pristine TiO_2, oxygen vacancy rich-TiO_2 (OV-TiO_2) and Cu-doped TiO_2 and 0.8% of intrinsic compressive strain using DFT + U, finding that oxygen vacancies decrease the band gap of pristine TiO_2 from 3.15 eV to 2.79 eV. In the OV-modified catalyst, new defect states in the middle of the band gap manifested while Cu doping divided the band gap of OV-TiO_2-strain (Cu-doped TiO_2) into two sections. Ru-doped $(TiO_2)_{1-12}$ nanocluster photocatalysts were studied by Žibert et al.[57] at the HSE06 level and found that the Ru atom narrows the band gap and introduces new mid-states due to Ru d orbitals. Partial DOS (pDOS) of TiO_2 and Ni-TiO_2 calculated by Li et al.[55] showed that the VBM mainly consists of O 2p states, while the CBM consists of Ti 3d orbitals. On the other hand, after Ni doping, new defect states are introduced into the structure of TiO_2 in the middle of the band gap and below the conduction band, where Ni 3d states have been observed to hybridize with O 2p states.

Using an older PW91 functional, Ye et al.[58] studied MoS_2@TiO_2 nanojunctions as a promising catalyst. Frontier orbital analysis of the charge transfer between TiO_2 and MoS_2 showed that the electrons are transferred from TiO_2 to MoS_2, while the HOMO orbital of the photocatalyst is mainly composed of TiO_2 and the LUMO is composed of MoS_2, especially Mo atoms.

4.1.2. g-C_3N_4 and other CN Catalysts

A second promising subset of NRR photocatalysts are g-C_3N_4 and other CN. The role of nitrogen vacancies was studied by

ChemSusChem

Review
doi.org/10.1002/cssc.202301730

Chemistry Europe
European Chemical
Societies Publishing

Ren et al.[59] with PW91+Hubbard to explore the optical properties, carrier mobility and separation of planar and corrugated NV-g-C_3N_4 photocatalysts, while the absorption spectra and electron transitions were calculated at the HSE06 level for central and 2-fold coordination NV catalysts. Transitions from n1 to π^* were shown to be forbidden in the pristine catalyst, but allowed upon the introduction of vacancies. The band gaps of corrugated catalysts are lower (2.33 and 1.80 eV for central and 2-fold coordinated NV catalysts, respectively) than those of the planar catalysts (2.53 and 2.50 eV for central and 2-fold coordinated NV catalysts, respectively) or pristine g-C_3N_4 2.68 eV. In addition, the recombination rates of photogenerated charge carriers showed that defects decrease the recombination and increase the separation efficiency.

Studying the activation of N_2 over pristine and Fe-doped g-C_3N_4, Yang et al.[60] showed that the VB of the pristine catalyst consists mainly of N 2p and C 2p levels and CB of N 2p states. After Fe doping, new localized Fe 2p states appear, which act as trapping centers. Furthermore, the DOS reveled that the orbitals of physically adsorbed N_2 on pristine g-C_3N_4 are very similar to the orbitals in an isolated N_2, implying that nitrogen is not activated on pristine catalyst.[61] On the other hand, upon nitrogen adsorption on Fe^{3+}-doped g-C_3N_4, the sigma 2p orbital (HOMO) of N_2 is delocalized, indicating nitrogen activation with the Fermi level N_2 of 7.32 eV. Overlapping d orbitals of Cu[62] or Co[63] with the antibonding π orbital of the adsorbed nitrogen molecule was also observed, confirming that the electrons are transferred from the Cu or Co active site to the activated adsorbed nitrogen.

On pristine, Bi-defected and single- or dual defected (K and —C≡N) g-C_3N_4, the band gap of the pristine catalyst (2.53 eV) is narrowed and the band structure changed from p-type to n-type. The distribution of electrons was determined from an electron localization function (ELF). Dual defects showed strong partial localization around K and —C≡N, respectively.

4.1.3. BiOX (X=Cl, Br, I) and BOC

Zhao et al.[65] employed the HSE06 approach to calculate the electronic and optical properties of pristine BiOCl, BiOCl/BiOBr, Mo-doped BiOCl and BiOCl/BiOBr. Based on the adsorption properties and reaction mechanism, Mo was identified as the most promising dopant. Undoped BiOCl, BiOBr and BiOI have indirect gaps of 3.80, 3.42 and 2.38 eV, respectively. Upon Mo-doping, a direct band gap with new defect levels was observed due to the band folding of the supercell. Due to impurity state below the CB after Mo doping of the heterojunction, the latter was chosen for the calculations of density of states, optical absorption spectra and MD simulations. DOS revealed that VB and CB stem from BiOCl and BiOBr, while the impurity states stem from Mo. The energy difference is high enough to effectively block carrier recombination. As seen in optical absorption spectra, heterojunctions or especially Mo doping enables the use of the visible light, while pristine BiOX catalysts have absorption peaks in the UV regime.

Charge carrier lifetimes for Mo-BiOCl and Mo-BiOCl/BiOBr were calculated using NAMD at 300 K to be 450 ps and 2 ns, respectively. In the latter case, electron and holes were trapped by the impurity states. On the other hand, in the Mo-BiOCl/BiOBr heterojunction, the electrons are transferred from the conduction band of BiOBr to the impurity states of Mo-BiOCl after 180 fs and the holes reach the impurity states after 3 ns. Charge separation and transport are fast and the recombination is suppressed for Mo-BiOCl/BiOBr, where the adiabatic mechanism prevails due to energy fluctuations of the impurity states up to 1.59 eV (Figure 5).

DFT−D3+U calculations of N_2 activation on BiOBr (102), examining the introduced OVs and the transition metals Fe, Mo, and Ni, showed an indirect band gap of 2.67 eV for the pristine structure,[66] while OV and metal doping introduce additional defect levels in the middle of the band gap. DOS showed that the CB of pristine catalyst consists mainly of Bi 6p states, while VB of Br states. The introduction of OV improves the electron-hole separation and similar results were shown by Di et al.,[67] who found new defect levels after the introduction of Bi vacancies in the single-unit-cell Bi_3O_4Br photocatalyst. DFT and AIMD simulations of O and Br vacancies in $Bi_4O_5Br_2$ (001) using implicit solvation found that the two oxygen vacancies are formed under UV light, while for the Br vacancy visible light suffices.[68]

Bi-ter BiOBr (001) and O-ter+H BiOBr (001) exhibited lowest cleavage energies. For Br-ter, Bi−Br, O-ter+H and OV−O-ter+H BiOBr (001) facets, the band gap values are 2.35, 1.72, 2.64 and 1.52 eV, indicating that introduced OV defects cause the narrowing of the band gap and might improve photocatalytic activity. PDOS revealed that the CB of different BiOBr atomistic terminations consists mainly of 6p states of Bi atoms, while the VB consists of 4p states of Br atoms and 2p states of O atoms. Br-ter facet exhibited the highest work function of 7.50 eV, followed by the BI−Br facet with the work function of 3.50 eV. OV−O-ter+H exhibited the lowest value of 2.88 eV and was together with Bi−Br facet the most promising for N_2 activation.
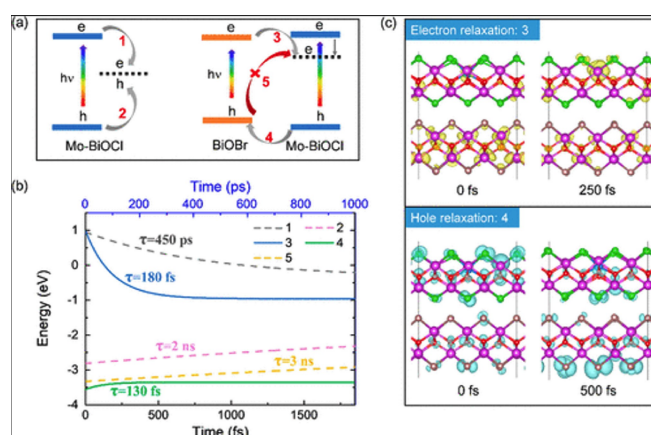

Figure 5. (a) A scheme of Mo-doped BiOCl heterojunction photocatalyst, (b) time-dependent energy change of electron-hole charge carriers obtained by NAMD simulations, and (c) charge density difference of electron and hole relaxation on Mo-BiOCl/BiOBr. Reprinted with permission from [65]. Copyright 2020 American Chemical Society.

4.1.4. Other Oxides

Several other oxides exhibit semiconducting properties and photocatalytic activity. On OV-MoO$_3$ (001), new defect level were observed after the introduction of OVs, which act electron trappers and donors of electrons to adsorbed nitrogen. The OV modification contributed to the lower charge carrier recombination and higher separation efficiency.[69]

Dual active centers (Ru-SA and Mo^{n+}) were added to H$_x$MoO$_3$ and the formation energy of two oxygen vacancies is 0.956 eV lower in Ru/MoO$_3$ than in the pristine catalyst.[70] The calculated PDOS showed metallic features from the valence to the conduction band due to intercalation of H in MoO$_3$. Hui et al.[71] calculated the PDOS of the Sb$_2$O$_3$/W$_{18}$O$_{49}$ heterojunction and observed electron density around the Fermi level and a charge transfer of 0.25 e_0 from Sb to W$_{18}$O$_{49}$ after the introduction of OVs. Dong et al.[72] calculated charge density distribution of W$_{18}$O$_{49}$, Fe/W$_{18}$O$_{49}$ and P–Fe/W$_{18}$O$_{49}$ and showed a stronger hybridization between W-d states and N$_2$ after Fe-doping.

Liu et al.[73] studied NRR over pristine and La-anchored MoO$_{3-x}$ using PBE + U. They found that the terminal oxygen vacancy in MoO$_{3-x}$ is thermodynamically most feasible, serving as an anchoring site for the single La atom.

Zhang et al. calculated the work functions and Fermi levels of BiVO$_2$ (6.66 eV and −5.74 eV, respectively) and ZnIn$_2$S$_4$ (4.59 eV and −4.95 eV, respectively) in the BiVO$_2$/ZnIn$_2$S$_4$ Z-scheme heterojunctions. They found that CB is located in ZnIn$_2$S$_4$, while VB consists of BiVO$_2$, indicating the photo-generated electrons are transferred from BiVO$_2$ to ZnIn$_2$S$_4$.[74]

4.1.5. Layered Double Hydroxides and Metal Organic Frameworks

Zhao[75] showed that when OV and OV with 1 % of compressive strain are introduced into pristine CuCr-LDH and ZnAl-NS, new defect levels around the Fermi level appear, suggesting that both act as electron trapping sites. Similarly, Zhao et al.[76] studied the band structure and charge density difference of pristine ZnCr, OV-ZnCr-LDH, Zn-OV-ZnCr-LDH and observed lower band gaps of modified catalysts (2.40, 2.19 and 2.18, respectively).

Metal organic frameworks as photocatalysts for nitrogen reduction were used by Zhang et al.[77] and Hu.[78] It was shown that the VB states consist of O 2p and C 2p orbitals, while Ce 4f orbitals predominant in the CB. Upon adsorption of N$_2$ at the active sites of Ce-CUS, the Ce 4f orbitals overlap with the pi anti-bonding orbital of N$_2$, indicating an electron transfer from Ce to N$_2$, activating the nitrogen triple bond to 1.117 Å. The Ce is involved in the electron-back donation process with N$_2$. Studying the nitrogen activation on Gd-IHEP-7 (2D MOF) and Gd-IHEP-8 (3D MOF), Hu[78] calculated a lower band gap (0.71 eV) than 2D MOF (0.69 eV) and a lower position of the HOMO level (−0.784 eV for 3D vs −2.669 eV for 2D MOF). Methyl-modification of pristine MOFs increased the band gaps (2.13 eV for 2D MOF and 1.90 eV for 3D MOF). This was one of the few studies where time dependent DFT (TD-DFT) calculations were used to verify the stability of the ground-state optimized structures of Gd-IHEP-7 and Gd-IHEP-8 in the excited state.

4.1.6. Sulfides

Upon Fe deposition on the surface of MoS$_2$, three 4-membered FeSMoS rings were formed and the stability of the Fe–S bonds near the water monolayer was confirmed by NVD MD simulations at the room temperature,[49] showing a binding energy of −4.28 eV. Density of states, calculated for pristine and Fe-deposited catalysts, showed additional states (occupied and unoccupied) around the Fermi level.

In pristine and Zn-defective Zn$_3$In$_2$S$_6$, a direct band gap of 1.28 eV was calculated at the gamma point,[79] while the band gap at the Z-point of a Zn-defective Zn$_3$In$_2$S$_6$ (S-TAA) was 1.56 eV. The VBM consists mainly of Zn 4s, 3p states, S 2p and In 5s states, while the CBM consists of S 3p and Zn 3d states. TiO$_{2-x}$S$_y$ with OV and sulfur dopants was studied by Xue et al.,[80] finding band gaps for Ti$_{16}$O$_{29}$S$_2$ (101), Ti$_{16}$O$_{27}$S$_4$ (101), Ti$_{16}$O$_{29}$S$_1$ (101) and Ti$_{16}$O$_{26}$S$_4$ (101) (OV and S defects: 2OV + 4S, 2OV + 8S, 4OV + 2S and 4OV + 8S, respectively) to be 0.97, 0.95, 0.98 and 0.55 eV, respectively. The presence of OV and S dopant atoms caused a narrowing of the band gap.

4.1.7. Other Photocatalysts

Lastly, we turn our attention to photocatalysts that do not fall in any of the aforementioned groups, such as plasmonically active Au$_4$Ru$_2$ clusters[81] with a DOS-calculated band gap of 1.25 eV, which agrees with the optical gap (1.33 eV) obtained from the photon energy scale spectrum. PDOS showed that LUMO and LUMO + 1 states are mainly composed of Ru atoms, confirming that Ru atoms serve as active sites for the adsorption of nitrogen molecule. For Pt-SACs/CTF photocatalysts, AIMD simulations at 300 K confirmed the thermodynamic stability of PCTF-PDDA-TPDH stabilized by three Pt–N bonds, showing the binding energy of −4.35 eV for the incorporation of Pt into the structure of the PCTF-PDDA-TPDH nanosheet.[47]

Band structures, DOS and work functions were calculated by Li et al.[82] for PaI, Fe$_2$O$_3$, and 30 % Fe-PaI at the PBE + U level. Due to a wide band gap of 3.52 eV for PaI, the electron excitation in the latter catalyst was excluded. On the other hand, 30 % Fe-PaI exhibited the lowest band gap of 0.98 eV and Fe$_2$O$_3$ of 2.78 eV. DOS showed that Fe-doping promotes electron excitation, while additional defects states appear below the CBM. The work functions of PaI, 30 % Fe-PaI and Fe$_2$O$_3$ were calculated to be 3.73, 3.85 and 4.62 eV, respectively, implying that the Fermi level of the Fe-doped catalyst is higher compared to the Fe$_2$O$_3$ catalyst. Furthermore, 60 % Fe-PaI was considered as a direct Z-scheme photocatalyst.

Pei et al.[83] performed one of the most extensive theoretical studies, coupling first-principles calculations with AIMD and ab initio nonadiabatic molecular dynamics to study black (BP) and

ChemSusChem

Review
doi.org/10.1002/cssc.202301730

Chemistry Europe
European Chemical
Societies Publishing

blue (BuP) phosphorene, confirming the thermal and water stability in simulation runs of 10 ps at 500 K. The formation energies of the vacancy defects were calculated to be 1.54–2.57 eV for BP and 2.49–2.81 eV for BuP, respectively. The band gap of pristine BP was determined to be 0.96 eV, changing negligibly for DV defective-BP. A pristine BuP exhibits the band gap of 2.67 eV, which is reduced by 0.69 and 0.50 eV when two different DV defects are introduced. After introducing defects, (additional) impurity levels appear and the charge density is localized between these impurity levels and the CBM. Furthermore, *ab initio* non-adiabatic MD simulations examined the lifetime of photogenerated charge carriers in defective phosphorene, showing the timescales of electron relaxation from the initial state to the impurity state of defective BP and BuP at 491.5 and 1107.6 fs. Moreover, the calculated Fourier transform of the band gap fluctuation showed the phonon model and the determined intermediate frequencies for DV-BP and DV-BuP of $\sim$417 cm^{-1} and $\sim$50 cm^{-1}, respectively. Electron-hole recombination was determined for both defective photocatalysts on a timescale of $\sim$2.3 ps, which is much slower compared with proton transfer from the molecular cation of water to the water molecule (100 and 491.5–1107.6 fs).

4.1.8. The Big Picture

Although TiO$_2$, g-C$_3$N$_4$, and bismuth oxyhalides are the most commonly studied catalysts for photocatalytic NRR, sulfides, metal-organic frameworks (MOFs) and layered double hydroxides (LDHs) should not be neglected. A vast majority of first-principles studies of the structure and electronic properties remain at the rudimentary ground-state level, often at the GGA (PBE or even PW91) level only, even though they struggle with underestimation of electronic properties.[36] Often, the Hubbard U-correction or the Grimme vdW corrections are included. While using hybrid functionals is an improvement, this is done exceedingly rare and mostly for stand-alone theoretical studies on account of the computational cost. Furthermore, the most commonly computed quantities are band gaps and the full band structure, charge densities and charge differences, work functions etc. Electronic properties are determined by calculating the band structure, density of states, and projected density of states. The band gap and the energies of the band edges (valence band maximum and conduction band minimum) are derived from the band structure and the total density of states. On the other hand, the projected density of states gives information about the orbital composition of CBM and VBM. They are summarized in Table 2.

4.2. Adsorption

The first step in the reaction mechanism is adsorption, which needs to be neither too weak nor too strong to avoid catalyst poisoning as epitomized by the Sabatier principle.[87] Furthermore, adsorption energies often serve as useful proxies for catalyst performance due to their correlation to the activation energies (Brønsted-Evans-Polanyi (BEP) relation).[57,88,89] For nitrogen reduction, adsorption of N$_2$, H$_2$, H$_2$O, and NH$_3$, N$_2$H$_4$ is most commonly evaluated. In addition to pristine catalysts, various defects, modifications and vacancies are considered when studying adsorption. Regrettably, only ground-state calculations are usually performed. In the following sections, first-principles studies of adsorption are grouped according to the catalysts studied.

4.2.1. Pristine and Modified TiO$_2$ Photocatalysts

Oxygen vacancies are the most common defects in TiO$_2$ and have received considerable attention for their role in nitrogen adsorption,[90,54,91,92] Using a combined HSE06+D3//PBE+U+D3 approach, the end-on adsorption of N$_2$ on OV and Ti$_{5c}$ active sites was found to be 0.26 and 0.30 eV more favorable compared to the side-on adsorption. Ti is the preferred adsorption active site yet it activates the molecule negligibly and the triple bond remains unperturbed. On hydroxygenated TiO$_2$, however, the end-on adsorption of N$_2$ is 0.61 eV more favorable and the triple bond is activated ($d_{N\equiv N} = 1.228$ Å). Through adsorption and photolysis of the first water molecule, the nitrogen molecule was found to be adsorbed at the OV sites and water molecules at the Ti active sites, even though the adsorption energies of H$_2$ over Ti and OV sites are similar.

Studying nitrogen activation over pristine and OV-defective TiO$_2$ NBAs (101), Zhang *et al.*,[54] calculated the adsorption energies of nitrogen over the Ti active site of OV-TiO$_2$ to be -0.44 eV, indicating. The electron transfer from Ti to nitrogen was observed and chemisorption confirmed by the elongation of the triple bond from 1.078 to 1.132 Å. Similarly, Yang *et al.*[91] observed a remarkable charge density difference and back donation, and a triple bond elongation from 1.109 to 1.162 Å on OV-defective catalyst. However, negligible electron transfer from pristine TiO$_2$ to nitrogen was observed by charge density calculations. The important role of OVs in activating the nitrogen molecule was observed by Zhang *et al.*,[92] who investigated the chemical adsorption of N$_2$ on the OV-modified anatase (101). The adsorption of nitrogen via an end-on configuration is most feasible on the OV active site with an energy of -1.09 eV. The increase electron density at the Ti atoms near OVs is transferred into the unoccupied antibonding orbital of N$_2$, while no activation of N$_2$ occurs at Ti atoms further from OVs.

Ixygen vacancies affect the polarization and activation of N$_2$ on all surfaces, with its adsorption energies on pristine TiO$_2$ (101), OV-TiO$_2$ (101), Ti$_3$C$_2$O$_2$, and OV-Ti$_3$C$_2$O$_2$ being -0.18, -0.62, -0.34, and -0.38 eV, respectively,[93] which correlate with the calculated charge density differences of 0.011, 0.210, 0.002, and 0.060 e_0, respectively. Guan *et al.*[94] also studied OV-TiO$_2$ (101) and F-modified TiO$_2$ (101), showing that N$_2$ adsorbs at the OV with an energy of -0.47 eV and receives 0.52 e_0, which activates it (bond elongation from 1.09 to 1.18 Å). There is little difference between pristine TiO$_2$, F-capped on the pristine surface, and on F added to the OV of TiO$_2$ (101) with

ChemSusChem

Review
doi.org/10.1002/cssc.202301730

Chemistry Europe
European Chemical
Societies Publishing

Table 2. A review of theoretical and experimental band gaps of photocatalysts for nitrogen fixation.

Catalyst	Functional	Theoretical band gap [eV]	Experimental band gap [eV]	References
pristine TiO_2	GGA-PBE, DFT+U	3.15	3	[53]
OV-doped TiO_2		2.79	/	
Cu-doped OV-TiO_2		/	3	
$(TiO_2)_{1-12}$	GGA-PBE	1.86–3.50	/	[57]
	HSE06	3.66–5.21	/	
Ru-$(TiO_2)_{1-12}$	GGA-PBE	0.26–1.46	/	
	HSE06	2.16–2.85	/	
g-C_3N_4	GGA-PBE, DFT–D2	3.21	/	[84]
B-doped g-C_3N_4		0.63 eV	/	
pristine g-C_3N_4	PW91, DFT–D, HSE06	2.68	/	[59]
planar NV (central)-g-C_3N_4		2.53	/	
planar NV(2-fold coordinated)-g-C_3N_4		2.5	/	
corrugated NV(central)-g-C_3N_4		2.33	/	
corrugated NV(2-fold coordinated)-g-C_3N_4		1.8	/	
pristine C_2N	GGA-PBE, DFT–D2	1.41	/	[85]
B/C_2N		0.6	/	
pristine BiOCl	HSE06	3.8	/	[65]
pristine BiOBr		3.42	/	
pristine BiOI		2.38	/	
BiOCl/BiOBr		/	/	
Mo-doped BiOCl		/	/	
Mo-doped BiOCl/BiOCl		/	/	
pristine BiOBr	DFT–D3, DFT+U (U=3.3, 8.6 and 3.4 eV for Fe, Mo and Ni)	2.67	/	[66]
OV-BiOBr		/	/	
Fe-BIOBr		/	/	
Mo-BIOBr		/	/	
Ni-BIOBr		/	/	
Mo-OV-BIOBr		/	/	
Ni-OV-BIOBr		/	/	
Br-ter BiOBr (001)	PBE-sol, PBE, DFT-D	2.35	/	[86]
Bi–Br BiOBr (001)		1.72	/	
O-ter+H BiOBr (001)		2.64	/	
OV–O-ter+H BiOBr (001)		1.52	/	
pristine CuCr-LDH	DFT+U	1.6	/	[75]
MgAl-NS		/	5	
ZnCr	GGA-PBE, DFT+U	2.4		[76]
ZnCr-LDH		/	2.51	
ZnCr-LDH-OV		2.19	ZnCr-1 h: 2.32	
ZnCr-OV–Zn		2.18	/	
Gd-IHEP-7 (2D MOF)	PBE, UPBE–D3	0.714	/	[78]
Gd-IHEP-8 (3D MOF)		0.691	/	
Gd-IHEP-7 ligand gr replaced with CH_3		2.126	/	
Gd-IHEP-8 ligand gr replaced with CH_3		1.904	/	
$Zn_3In_2S_6$ (S-TA)	GGA-PBE	1.28	2.78	[79]
N-defective $Zn_3In_2S_6$ (S-TAA)		1.56	/	
S-Cys ($Zn_3In_2S_6$ from L–CYS)		/	2.89	
S-TA ($Zn_3In_2S_6$ from TA)		/	2.81	

ChemSusChem

Review
doi.org/10.1002/cssc.202301730

Chemistry Europe
European Chemical
Societies Publishing

Table 2. continued					
Catalyst	Functional	Theoretical band gap [eV]	Experimental band gap [eV]	References
$Ti_{16}O_{29}S_2$ (101)	GGA-PBE, DFT–D3, HSE06 for bandgap	0.97	/	[80]
$Ti_{16}O_{27}S_4$ (101)		0.95	/	
$Ti_{16}O_{29}S_1$ (101)		0.98	/	
$Ti_{16}O_{26}S_4$ (101)		0.55	/	
$Ti_{32}O_{52}S_8$		/	1.18	
$Ti_{32}O_{61}S_2$		/	3.22	
anatase OV-TiO_2 (101)	GGA-PBE, DFT–D3	/	/	[81]
Au_2Ru_2		1.25	1.33	
Ag_4Ru_2/OV-TiO_2 (101)		/	/	
$Au_4Ru_2(SCH_3)_8$ $(P(CH_3)_3)_2$ /TiO_2		/	/	
black phosphorene (BP)	GGA-PBE, HSE06	0.96	/	[83]
DV-BP		0.98–1.00	/	
blue phosphorene (BuP)		2.67	/	
DV-BuP		1.98–2.17	/	

the adsorption energies of −0.25, −0.29, and −0.31 eV, respectively.

Fe-doping is commonly used and was heavily investigated.[56,95] The adsorption over Fe^{3+} doped anatase TiO_2 (101) is thermodynamically favorable in the end-on configuration with the energy of −0.62 eV. Wu *et al.*[56] showed a similar effect over Fe- and OV–Fe-doped TiO_2 (101) with the side-on adsorption of −1.70 eV on the OV–Fe-doped catalyst and −1.47 eV on the pristine Fe-doped catalyst, activating the nitrogen molecule (bond elongation to 1.234 Å). While the absolute values of adsorption energies vary wildly between different methods and approaches, Fe-doping has always shown to improve adsorption. Cu-doping was also shown to have a similar affect,[53] which eclipses the effect of OVs.

The effect of heterodopants was also investigated for Ru,[57] Ni,[55,96] Au[81] and carbon.[97] On $(TiO_2)_n$ nanoclusters, there is a clear inverse relationship between the cluster size and adsorption strength. Ni dopants also improve the adsorption (−0.53 eV vs. −0.25 eV for pristine TiO_2). Furthermore, Ni doping introduces OVs that act as electron trapping centers, increasing the photocatalyst performance. Using PBE+U+D3 (U = 4.5 eV for Ti 3d), Gao *et al.* computed weak adsorption energies on TiO_2(101)/Ni (−0.38 eV), TiO_2 (101) (−0.36 eV) and TiO_2(101)/Pt (−0.34 eV) in comparison to that on MXene (−1.34 eV) or TiO_2/Fe (−0.86 eV).

Sun *et al.*[81] studied the anatase TiO_2 (101), Au_4Ru_2/TiO_2 (101) and $Au_4Ru_2(SCH_3)_8$ $(P(CH_3)_3)_2$/TiO_2 (101) photocatalysts. On the Ru active site, end-on adsorption is most feasible (−1.33 eV), including electron transfer and a slight N≡N bond elongation. On $Au_4Ru_2(SCH_3)_8(P(CH_3)_3)_2$, no effect on N_2 activation was found (adsorption energy of −0.28 eV per Au(Ru)). On OV-$BaTiO_3$(110), nitrogen is adsorbed with an energy of −4.60 eV.[98]

Comer *et al.*[97] substituted a bridging oxygen atom for a carbon radical (C*), considered an active site for N_2 adsorption formed from methane (CH_4) during photooxidation. While C* active sites have a strong N_2 binding energy of −1.89 eV, they are reported to be unstable.

The electronic properties of TiO_2 catalysts can be improved by introducing oxygen vacancies, incorporating different dopant atoms (Fe, Ru, Ni, Pt, Co), creating MXenes or heterojunctions. The introduction of different dopant atoms improves the adsorption energies and activates the nitrogen triple bond.

4.2.2. g-C_3N_4 and other CN Catalysts

Ren et al.[59] studied nitrogen adsorption over planar and corrugated central and 2-fold coordinated catalysts NV-g-C_3N_4 at a PW91+D level, calculating an adsorption interaction of 2.56 eV in a side-on configuration on the NV active site with the accumulation of electrons in the 2p* orbitals of N_2 and depletion in σ 2p orbitals of NV. A higher charge transfer from the catalyst to the adsorbed nitrogen was observed at the corrugated 2-fold coordinative NV (0.19 "e_0") than from the corrugated central NV (0.09 e_0). Only one of the investigated NV sites on NV-g-C_3N_4 was found to be suitable for nitrogen adsorption (−166.2 kJ/mol) by Ma *et al.*,[99] where the nitrogen triple bond is activated (increased from 1.107 to 1.242 Å). On NV-rich g-C_3N_4, one nitrogen vacancy site (denoted as position 1) was found to be the most promising for nitrogen chemisorption (−166.2 kJ/mol), while the other was inert (−2.4 kJ/mol).[100] Dong *et al.*[101] studied NV-g-C_3N_4 (bulk and (001) surface) and also observed nitrogen activation upon adsorption at OV.

In Figure 6, the three different adsorption sites on g-C_3N_4 are shown: oxygen atom, hydroxyl group in a OV-rich catalyst, and pristine g-C_3N_4 (denoted as A, B and C, respectively). Shi *et al.*[102] found that adsorption at the C site is most favourable. Additionally, the adsorption energies at the less favourable sites
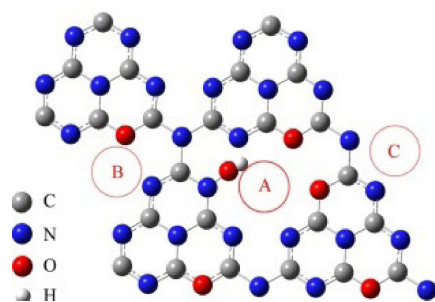
ChemSusChem

Review
doi.org/10.1002/cssc.202301730

Chemistry
Europe
European Chemical
Societies Publishing

Figure 6. Three adsorption modes on vacancy-rich g-C$_3$N$_4$ for N$_2$ adsorption, denoted as A, B and C. Reprinted with permission from [102].

A and B increase 2-3 fold upon the introduction of oxygen atoms or OH groups into g-C$_3$N$_4$.

On VN-gC$_3$N$_4$ and VN–S-g-C$_3$N$_4$, the nitrogen adsorption and activation on VN sites is stronger at −3.52 and −4.54 eV and 1.331 and 1.415 Å, respectively.[103] The electron transfer from the NV to the antibonding orbital is slightly increased in the presence of S. Similarly, sulphur-doped g-C$_3$N$_4$ with carbon vacancies (SCNN-550) was shown to adsorb nitrogen at carbon vacancies (−0.665 eV) compared to bulk sulphur-doped g-C$_3$N$_4$ (−0.335 eV).[46] Phosphorous can also be added to improve adsorption.[104] Using PW91 with an OBS method, nitrogen chemisorption over VN–P was computed to be −4.72 eV compared to −3.52 eV on a P-free catalyst. A charge transfer analysis confirmed that P positively affects the nitrogen vacancies to donate electrons to the adsorbed nitrogen.

Similarly, Fe doping improves nitrogen adsorption, which is increased from 1.587 eV to 1.911 eV over Fe-doped g-C$_3$N$_4$ photocatalysts along with the triple bond activation (elongation from 1.11 Å to 1.19 Å).[60] There are considerable difference between different approaches with Hu *et al.* calculating the adsorption interaction increasing from −0.151 eV to −1.397 eV[61] upon Fe-doping.

The free energy change in the HER process and the adsorption energies on the Fe-EDTA g-C$_3$N$_4$ (CNNS) nanosheets at the GGA level showed a cooperative effect of Fe and EDTA −0.26 and −0.29 eV for CNNS and EDTA-CNNS, respectively) and chemisorption (−0.99 eV for Fe-EDTA-CNNS).[105]

Transition metals have also been studied extensively, including Mo, Co, Cu. Immobilized single atom Mo on g-C$_3$N$_4$ adsorbs nitrogen in an end-on configuration (−1.31 eV),[106] while a water molecule binds with an interaction of −0.39 eV. Using the PW91 functional, Co-doped g-C$_3$N$_4$ was found to adsorb nitrogen strongly (−156.5 kJ/mol) but activating the triple bond moderately (increase from 1.175 to 1.178 Å). A Hirshfeld charge analysis revealed that the Co is present as a cation with a charge of +0.25. On M$_S$-Cu-g-C$_3$N$_4$, the adsorption strength upon nitrogen activation is −1.196 eV, brought about by a charge transfer from Cu$^+$ to N$_2$.[62]

Dual defected (K and −CN≡N) g-C$_3$N$_4$ were to adsorb nitrogen at the −CN≡N active site with an adsorption energy of −1.72 eV. A large electron transfer to the K site from the adsorbed N$_2$ (1.33 e_0) was observed, while the −CN≡N site donates 0.47 e_0.

Going beyond single atom doping, Liu *et al.*[107] studied Ru$_{11}$ clusters on a E-g-C$_3$N$_4$ layer and on the edges of the two layers of B-g-C$_3$N$_4$, observing an interaction of −2.18 eV for N$_2$ with an end-on configuration over Ru/E-g-CN. An end-on configuration is 0.83 eV more stable than a side-on configuration.

Liang *et al.* looked at pristine g-C$_3$N$_4$ (CN), ultrathin carbon nitride with (UCNx) and without nitrogen vanacies (UCN) and boron-doped ultrathin carbon nitride with nitrogen vacancies (BNUCNx–B1 and BNUCNx–B2).[108] Among those, BNUCNx–B2 adsorbs nitrogen most strongly (−0.81 eV) in comparison to the other catalysts (−0.21 eV or less). This corresponds to the activation of the triple bond (to 1.26 Å vs. 1.16 Å (UCNx) and 1.223 Å (BNUCNx–B1). The Mulliken charge analysis revealed that the nitrile group (−CN) acts as an electron acceptor and that the B atom facilitates the electron transfer to N$_2$ with the Mulliken charges for B in BNUCNx–B1 and BNUCNx–B2 of 0.98 e_0 and 0.96 e_0, respectively.

A larger screening study was performed by Yang *et al.*[109] using spin-polarized DFT–D3 calculations, looking into M$_4$@B$_{36}$N$_{36}$ clusters. After proposing 11 metals to be caged into the B$_{36}$N$_{36}$ structure (Sc, Ti, V, Cr, Y, Zr, Nb, Mo, Hf, Ta and W), 8 were ultimately included in the cluster structures for their affinity to the side-on N$_2$ adsorption. Adsorption energies between −0.01 and 0.89 eV and a charge transfer of 0.41–0.55 e_0 were observed along with modest nitrogen bond activation (elongation for 0.09 and 0.12 Å). Y$_4$@B$_{36}$N$_{36}$ exhibited the lowest adsorption energy of −0.76 eV and highest charge transfer (0.72 e_0) but was was excluded from further studies due to stability issues (structural distortion upon N$_2$ adsorption).

Liu *et al.*[110] studied GaN NW with nitrogen vacancies due to its high surface activity and stability. They showed that N$_2$ physisorbs on pristine GaN, while nitrogen vacancies promote chemisorption with an activated triple bond (elongated to 1.28 Å) due to electron transfer from Ga to the N$_2$ antibonding orbitals. Bader charge analysis shows that effectively N$_2^-$ is formed.

Lastly, Bhattacharyya *et al.*[85] simulated free nanoporous carbon nitride B/C$_2$N at the PBE+D2 level. N$_2$ adsorbs preferentially end-on at the B active site of B/C$_2$N (−1.44 eV) rather than side-on (−0.58 eV). However, the triple bond is more elongated in the latter case (1.21 Å vs 1.14 Å), prompting the authors to investigate both possibilities mechanistically.

4.2.3. BiOX (X = Cl, Br, I) and BOC

Pristine, OV-modified and doped BiOX (X=Cl, Br) were studied by Zhao *et al.*,[65] Wu *et al.*,[111] Li *et al.*,[112] Xue *et al.*,[113] Li *et al.*[114] and Liu *et al.*[86] Among 3d, 4d, and 5d transition metal-doped BiOX (X=Cl, Br), Mo-BiOCl was showed the lowest adsorption energy of −1.42 eV and triple bond activation (to 1.16 Å).[65] Differential charge density showed an accumulation of electrons on N$_2$. While pristine BiOCl (001) was conducive to HER, it did not occur on the doped surface.

A significant role of oxygen vacancies was shown by Wu *et al.*,[111] confirming nitrogen activation on OV-BiOCl (001) (triple bond elongation to 1.173 Å). Br doping further activated

ChemSusChem

Review
doi.org/10.1002/cssc.202301730

Chemistry
Europe
European Chemical
Societies Publishing

the triple bond (1.184 Å). On the (010) and (001) facets, a similar effect is seen.[112] A Bader charge analysis revealed that more electron density accumulates on N_2 in the case of OV-BiOCl (010) (a Bader charge of nitrogen adsorbed on OV-BiOCl (010) is 11.15 e_0) than for OV-BiOCl (001). Similarly, Xue et al.[113] and Li et al.[114] confirmed a beneficial role of oxygen vacancies in OV-rich BiOBr (001) for N_2 activation.

Over Bi–Br and OV–O-ter+H, electron transfer using the Hirshfeld charge analysis, charge density difference, and N_2 adsorption energies showed[86] that for both facets the end-on adsorption configuration is more stable (0.15 eV on Bi–Br and −1.90 eV on OV–O-ter+H). Adsorption of O_2 and H_2 was also studied and the results showed higher adsorption energies for hydrogen than for oxygen.

Liu et al.[115] studied the formation of OV in Fe-doped BiOBr at the PBE level and calculated their formation energy as 2.45 and 3.30 eV when connected with Fe and Bi, respectively, indicating that they form near Fe in Fe-BiOBr. Charge density calculations showed that in pristine BiOBr, oxygen atoms active sites for nitrogen adsorption, while doping Fe assumes this role. At the PBE+D3+U level (U=3.3, 8.6 and 3.4 eV for Fe, Mo and Ni, respectively), Chen et al. studied[66] nitrogen adsorption over defective and pristine BiOBr (102) surfaces. Among pristine BiOBr, OV-BiOBr, Fe-BiOBr, Mo-BiOBr, Ni-BiOBr, Fe—O-BiOBr, Mo—O-BiOBr and Ni—O-BiOBr, Ni-OV-BiOBr adsorbs nitogen most strongly (−0.45 eV), while the most efficient charge transfer occurs from Fe-OV-BiOBr (102), where the triple bond is most activated (to 1.142 Å). Experimentally, Fe-OV-BiOBr is confirmed to be the most suitable.

On pristine and BiOV-defective Bi_3O_4Br, nitrogen adsorbs weakly (−0.087 vs. −0.241 eV, respectively) since no dispersion corrections were employed.[67] Among Bi_5O_7Br, Bi_5O_7Br+O (additional O atom), OV-Bi_5O_7Br, OV-$Bi_{12}O_{17}Br_2$, BrV-$Bi_4O_5Br_2$ (001), no noticeable differences are observed (−0.008, −0.017, −0.001, −0.017, −0.03 eV, respectively).[116,117]

4.2.4. Other Oxides

The role of OVs was studied on MoO_3 by Li et al.[69] using at the PBE+U+D2 level, calculating the Mulliken charges, DOS, Bader analysis and N_2 adsorption. Based on the Mulliken charges of 1.44 and −0.451 for Mo and O atoms, respectively, in pristine MoO_3, and 1.37 and −0.499 in OV-MoO_3, and the Mo—O binding energies in Mo_4O_{11} (7.64 eV) and Mo_4O_{12} (8.52 eV), nitrogen adsorption on the OV on (001) and (100) was posited. On OV-MoO_3 (001), nitrogen adsorbs in a side-on configuration and on (100) in an end-on configuration, extending the triple bond to 1.152 and 1.157 AA, respectively. The higher activation on OV-MoO_3 (001) was confirmed with a Bader charge transfer of 0.34 e_0 in the former compared to 0.09 e_0. In La-loaded $MoO_{3−x}$ photocatalysts, La significantly improves nitrogen adsorption in a side-on configuration.[73] DOS analyses shows that during N_2 adsorption, the electrons are transferred from the 5d orbitals of La to the π antibonding orbital of N_2.

In Fe-doped WO_3, Fe atoms improve N_2 adsorption (from −0.28 to −0.59 eV) and activate it.[118] On the other hand, Mo-

doping of $W_{18}O_{49}$ causes a strong end-on adsorption of N_2 on the Mo atom (−2.48 eV vs. −1.65 eV for the non-doped) and greater activation (charge transfer increases from 0.45 to 0.58 e_0).[119] On β Ga_2O_3 (111), an adsorption energy of −0.97 eV was found and the photogenerated electrons were transferred directly or through carbonaceous radicals.[120]

Similarly, a heterojunction increased N_2 adsorption interaction to −1.08 eV compared to separate Sb_2O_3 (−0.35 eV) and $W_{18}O_{49}$ (−0.45 eV).[71] A differential charge density and Bader analysis showed a charge transfer of 0.75 and 0.53 e_0 from the Sb and W sites to N_2, respectively. Moreover, the OVs in $W_{18}O_{49}$ act as trapping centers for the photogenerated electrons.

Lastly, Li et al.[121] compared nitrogen adsorption on non-polar (100) and (001), and polar (002) surfaces of OV- and Ti-doped $ZnO_{1−x}$. Polar Ti-$ZnO_{1−x}$ (002) exhibited the strongest adsorption interaction (−0.47 eV) and bond activation (to 1.328 Å) as 1.28 e_0 is transferred to N_2. On $W_{18}O_{49}$, Fe/$W_{18}O_{49}$, and P–Fe/$W_{18}O_{49}$, the P–Fe codoping improves adsorption (−0.91 eV −0.35 eV for $W_{18}O_{49}$) and activation (bond length of 1.39 Å) the most.[72]

4.2.5. Layered Double Hydroxides and Metal Organic Frameworks

In OV-defective CuCr-LDH and ZnAl-LDH, introduction of strain improves nitrogen adsorption, reaching −0.886 eV on OV-strain CuCr-LDH and −1.080 eV on OV-strain-ZnAl-LDH.[75] On OV-ZnAl-LDH and Cu ($Cu^{\sigma+}$)-doped OV-ZnAl-LDH, the adsorption interaction of −0.94 eV was calculated at a PBE+U level.[122] Bader charge calculations showed that the Bader charge of the unsaturated Cu atom (0.16 e_0) was lower than that of the Cu atom (0.21 e_0) in pristine ZnAl-LDH, confirming electron accumulation on Cu in 0.5 %-ZnAl-LDH. A significant charge density difference was observed between the Cu atom and OV when OV were introduced and Cu doped into the ZnAl-LDH structure. Nitrogen adsorbs more easily on unsaturated Zn active sites of ZnCr-LDH (−0.45 eV) than on saturated Zn active sites (−0.17 eV).

The feasibility of Fe and Cr active sites in MIL-101(Cr) and MIL-101(Fe) was confirmed by Li et al.,[123] calculating an adsorption energy of −0.43 eV on the former and −0.48 eV on the latter, where a significant electron transfer from Fe to N_2 calculated was observed. Nitrogen adsorbs on Gd-IHEP-7 and Gd-IHEP-8 in an end-on configuration with interactions of −0.26 and −0.29 eV, respectively.[78] On Al-PMOF and Al-MOF (Fe), however no activation was observed at the PBE+D3 level and a most adsorption interaction of ∼−0.50 eV in an end-on configuration was seen.[124]

4.2.6. Sulfides

Adsorption of N_2 and H_2O on the Fe active site in Fe-MoS_2 was examined by Azofra et al.,[49] calculating an adsorption energy of −0.67 eV and 0.8 e_0 charge transfer from Fe to MoS_2 and from N_2 to Fe. On SV-CdS (111), nitrogen is chemisorbed and

ChemSusChem

Review
doi.org/10.1002/cssc.202301730

Chemistry Europe
European Chemical
Societies Publishing

activated (-126.5 kJ/mol, 1.213 Å)[125] as opposed to the pristine catalyst.

Liu et al.[126] performed broken symmetry DFT calculations to study the binding energies between N_2 and the unreduced and reduced (5-, 4-, 3-, 2- and 1- oxidation states) precursors of FeMoS-FeS-SnS, FeMoS-SnS and FeS-SnS. Nitrogen adsorption on unreduced $Mo_2Fe_6S_8(SPh)_3$ catalyst was found to be the most thermodynamically favorable with a binding energy of ~ 10 kcal mol^{-1}. It is further reduced when the chalcogel is reduced to 5- (by ~ 7 kcal mol^{-1}. The adsorption on the Fe active site showed similar results. The authors concluded that 5-reduced states are most favorable for nitrogen fixation.

Studying BPNS/CdS (0001), Shen et al.[127] through charge density difference at the interface found efficient charge separation, while nitrogen was only weakly adsorbed (-0.11 eV). On CdS(002), NiS(211) and Ni-doped CdS surface, the adsorption energies were 1.16, -0.26 and -0.55 eV, respectively.[128] Yuan et al.[22] found that among Ru(001), CoS$_x$ (101), and CoS$_x$ (101)/Ru(001) the Ru—Co center of the latter adsorbs nitrogen best (-1.01 eV) and activates its triple bond the most (1.239 Å). N_2 adsorbs over the Co—S center in a side-on configuration, whereas it is adsorbed in an end-on configuration on other catalysts.

Ma et al.[129] screened the anchoring of transition metal single atoms (Sc, Ti, V, Cr, Fe, Co, Ni, Cu, Nb, Mo, Te, Ru, Rh, Pd, Ag, Cd, W, Pt, Au) on the WS_2 monolayer with S-vacancy, calculating the most likely formation modes (S-vacancy or WS hexagonal ring) and nitrogen adsorption modes via end-on and side-on configuration. Ni was identified as most promising for nitrogen chemisorption as other metals bind N_2 or intermediates too strongly or too weakly. N_2 interacted negligibly with S-WS_2 (-0.04 eV), while its adsorption on the Ni active side was -0.92 and -0.69 eV and charge transfer of 0.12 e_0 and 0.09 e_0 in the end-on and side-on configuration, respectively. Mn-doped MoS_2 was studied by Hu et al.,[130] showing nitrogen adsorption on the Mn sites with an adsorption energy of -0.2 eV (on Mn-MoS$_2$-SV) and -0.44 eV (on Mn-MoS$_2$-2SV).

Lastly, Hue et al.[80] looked into the OV—S rich- and OV—S-poor $TiO_{2-x}S_y$ (101). In the latter case, $Ti_{32}O_{52}S_8$ and $Ti_{32}O_{61}S_2$ with 4 OV+8 S and 1OV and 2S were constructed, respectively. N_2 adsorption over OV—S-rich $TiO_{2-x}S_y$ was more feasible, with adsorption energies ranging from -0.76 to -2.1 eV as the amount of OVs increased. Surface S-doping proved that the latter position was energetically more favorable by 0.53 eV. In general, OV and S favorably affect the adsorption of N_2. Zhang et al.[74] investigated the adsorption of N_2 over the Zn, In, S atoms in a pristine $BiVO_2/ZnIn_2S_4$ Z-scheme heterojunction and on sulfur vacancies (SV) of SV-rich $BiVO_2/ZnIn_2S_4$. Photogenerated electrons are gathered in the CBs of $ZnIn_2S_4$ or SV-$ZnIn_2S_4$ and transferred to the adsorbed N_2, which is then activated. SVs promote nitrogen adsorption the most among all the tested adsorption active sites (In, Zn, S atoms).

4.2.7. Other Photocatalysts

On other photocatalysts, the adsorption energies vary vastly. On Pt-SACs/CTF, N_2 adsorbs at the N_3 site with an adsorption energy of -0.97 eV[47] as the electrons are transferred ($+0.43$ e_0) from the Pt atom (active site) into the CTF framework (the energy for the incorporation Pt atom into SACs/CTF is -4.35 eV).

Among the three actives sites of Fe_1O_4/C-PPH$_3$/Na and also on O_2/C and Fe_1O_4/C, nitrogen adsorbs most readily on Fe_1O_4/C (-1.59 eV), which is even more preferred than hydrogen adsorption (-0.80 eV).[131]

Qin et al.[132] investigated the Ti_3C_2 (001) surface and calculate the side-on adsorption energy of -5.20 eV for nitrogen, which is greater than for the end-on adsorption on the Ti—Ti tripolymer with the energies of -3.16 and -2.75 eV. In the process, the electrons are transferred from the d-orbital in Ti to the N_2 via an electron back-donation process, resulting in its activation (bond length 1.192 and 1.245 Å (end-on) or 1.334 Å (side-on).

Black (BP) and blue (BuP) phosphorenes activated the chemisorbed nitrogen molecule (interactions between 0.25 and 1.86 eV), while the triple bond in nitrogen was extended to 1.25–1.46 Å after an electron transfer of 1.20–2.00 e_0 from the defective phosphorenes.[83]

The important role of oxygen vacancies was shown by Li et al.,[133] who studied BMO (Bi_2MoO_6) and OV-BMO-OH (010). It was found that OVs significantly decrease the adsorption energy (-3.95 eV vs. -1.91 eV for pristine vs. OV-catalyst), which was also observed by higher triple bond elongation upon adsorption on OV-BMO-OH (010) (1.174 Å vs 1.209 Å for adsorption on pristine and OV-catalyst, respectively). The activation of the triple bond to 1.288 Å upon electron transfer from Bi_2WO_6 was also shown by Zhang et al.[134] Similarly, Sun et al.[135] found the Fe site in $LaFeO_3$ (121) as the most promising for nitrogen activation. The activation was explained as a pull and push process, which is depicted in Figure 7.

On Fe sites in $FeCo_2O_4$(311), nitrogen adsorbs with -0.78 eV, computed at the PBE+D3 level. There is considerable overlapping of Fe d orbitals with empty π orbitals of N_2 and
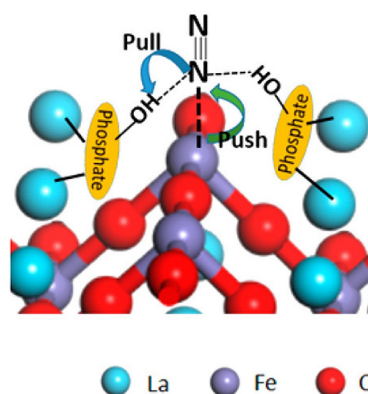

Figure 7. Pull and push process of N_2 activation over $LaFeO_3$. Reprinted with permission from [135]. Copyright 2017 American Chemical Society.

electron flow from Fe to N_2. Additionally, MD calculations were performed to show that the distribution of nitrogen molecules over the bulk catalyst is small.[136] On pristine boron doped and OV-modified HNb_3O_8 and $HNbO_3$, charge density calculations showed that N_2 is activated upon adsorption on the surface of B-OV-$HNbO_3$.[137] On OV-$InVO_4$, PBE+D3 showed the strongest adsorption energy when nitrogen is adsorbed on the V^{4+} active site (-0.96 eV) compared to adsorption on OV (-0.54 eV) or the In atom (0.03 eV).[138]

4.2.8. The Big Picture

N_2 adsorption plays an important role in photocatalytic NRR as it determines whether the reaction is plausible, as explained in Section 2.2. Physisorption is often too weak for the chemical reaction to occur, while a too strong adsorption leads to the poisoning of the catalyst surface, which negatively affects photocatalytic activity, as shown for dual-metals loaded g-C_3N_4 surfaces.[139]

In this section, we reviewed the computational approaches to N_2 adsorption and activation on different catalysts. In a vast majority of studies, the authors resort to computing the adsorption energies, charge transfer (Bader, Hirshfeld) and density, and bond elongation. The calculations are carried out in the ground state using standard GGA approaches, most commonly PBE or PW91 functionals, often using D3 corrections to account for the dispersion correction and Hubbard U on heavy atoms. This leaves out important insights with regard to the behaviour of excited catalyst and N_2.

Generally, nitrogen is adsorbed in an end-on or side-on configuration. While adsorption modes depend on the catalyst structure, it can be summarized that vacancies and dopant atoms (cocatalyst) are considered as active sites for N_2 adsorption. Upon the adsorption, electrons are transferred from the catalyst to the π antibonding orbital in N_2 and the triple bond in N_2 is prolonged, resulting in activation of the adsorbed molecule.[1,3,4,15] Calculated adsorption energies, theoretical properties, and reaction mechanisms are summarized in Table 3.

4.3. Reaction Mechanism

As discussed Section 2.1, nitrogen can be converted to ammonia through different mechanisms, depending on the adsorption configuration (end-on or side-on). The former facilitates the associative distal or alternating mechanism, and the latter favours the enzymatic mechanism. Theoretical studies have shown that the associative mechanism is much more common since it is more difficult to dissociate the nitrogen triple bond under photocatalytic conditions. There are comparatively few first-principles mechanistic studies dealing with the excited states inherent to photocatalysis. More often, ground state calculations are performed instead. Thus, all mechanistic studies reviewed below are, unless explicitly noted otherwise, performed at the ground state.

4.3.1. Pristine and Modified TiO_2 Catalysts

Xie *et al.*[90] NRR with water photolysis over pristine and hydroxylated rutile $TiO_2(110)$ using the HSE06+D3/PBE+U+D3 GGA-PBE approach. Consistent with the more feasible end-on adsorption of N_2 onto OVs, a distal to alternating reaction pathway was proposed with the N–N cleavage in *NH_2 as the rate-limiting step with a barrier of 1.28 eV. The overall reaction mechanism was exothermic with an energy of ~ -2.0 eV. Qian *et al.*[140] also studied the OV-TiO_2 photocatalyst. They suggested to start the NRR with a distal mechanism, continue with an alternating and finish with an enzymatic pathway. The formation of the second ammonia molecule is considered a potentially rate-limiting step with a barrier of 0.69 eV. Moreover, the OVs facilitate NRR by promoting charge transfer and N_2 activation. On the other hand, Zhang *et al.*[54] predicted the distal and alternating pathways for NRR over OV-TiO_2 NBAs (101) due to the end-on N_2 adsorption. The formation of the first ammonia molecule was the rate-limiting step in both pathways, but its formation is more feasible in the alternating pathway scenario ($+0.37$ eV) than in the distal pathway ($+1.53$ eV).

The role of Fe doping in TiO_2 was studied by Zhao *et al.*,[95] Wu *et al.*[56] and Comer *et al.*[149] While Zhao *et al.*[95] calculated only the adsorption energies of the intermediates along the alternating mechanism, Wu *et al.*[56] found that Fe doping promotes hydrogen transfer and decreases the Gibbs free energies during successive hydrogenation steps on TiO_2 (101). Over a pristine and Fe-doped catalyst, the first hydrogenation was found to be rate-determining with the Gibbs free energies of 1.270 and 0.930 eV, respectively. The reaction followed the enzymatic mechanism as nitrogen adsorbed via the side-on configuration on Ti active sites. Comer *et al.*[149] studied pristine, OV-defective and Fe-doped rutile $TiO_2(110)$ using the BEEF-vdw functional and calculated the surface free energy, coverage and coverage probability for H_2O, N_2, O_2 and OH. The dissociative and associative pathways were proposed and the free energy calculations indicated that dissociative nitrogen reduction was unfavourable due to high energy barrier of 8.5 eV for the rate determining step. The associative pathway was more favourable than the dissociative.

Often, initial hydrogenation of N_2 is considered rate-limiting and studied exclusively. Only the first two hydrogenations of N_2 on pristine, OV-defected and Cu-doped TiO_2 were studied by Zhao *et al.*,[53] finding the hydrogenation to N_2H* most challenging with the Gibbs free energies of 2.115 eV, 0.893 eV, and 0.365 eV on on pristine TiO_2, OV-TiO_2, and Cu-doped TiO_2, respectively. Comer *et al.*[97] the examined photooxidation of CH_4 to form C* radicals, which are incorporated into the structure of TiO_2. For the first ammonia formation, the researchers proposed a distal mechanism, where the potential-determining step was found to be the first hydrogenation of C*-N_2 to C*-N_2H with a barrier of 0.55 eV. The second ammonia was formed in simultaneous hydrogenation steps between the C active site and the remaining nitrogen atom. After desorption of the second ammonia molecule, C*H_3 is regenerated via photo-oxidation.

Table 3. A review of calculated adsorption energies, mechanisms, and other properties of nitrogen reduction over promising photocatalysts.

Catalyst	Functional	Molecular Dynamics	Adsorption energy [eV]	Mechanism	Calculated properties	References
rutile TiO_2 (110)	HSE06+D3//PBE+U+D3, GGA-PBE	/	end-on: 0.40, side-on: 0.10	/	N_2 adsorption energies, N_2 bond prolongation, reaction mechanism, charge transfer	[90]
OV-rutile TiO_2 (110)		/	end-on: 0.31, side-on: 0.05	/		
hydroxylated rutile TiO_2 (110)		/	end-on: 0.21, side-on: 0.10	/		
hydroxylated OV-rutile TiO_2 (110)		/	end-on: 0.61, side-on: 0.15	hybrid distal-dissociative		
OV-TiO_2	GGA-PBE	/	−0.43 (Gibbs free energy)	distal-alternating-enzymatic	reaction mechanism	[140]
anatase TiO_2 (101)	PBE, DFT+U (U=5.8 for Ti 3d)	/	/	/	band structure, CBM and VBM, DOS, electron density difference, N_2 adsorption, reaction mechanism	[54]
OV-anatase-TiO_2 (101) (DTiO_2 NBAs)		/	end-on: −0.44	distal, alternating		
pristine TiO_2 (010)	GGA-PBE	/	/	/	charge density difference, N_2 bond prolongation, electron transfer (working in tandem), back donation	[91]
OV-TiO_2 (010)		/	/	/		
pristine anatase TiO_2 (101)	PBE, DFT+U	/	/	/	Bader charge, differential charge densities, N_2 adsorption energies, N_2 bond prolongation	[92]
OV-anatase TiO_2 (101)		/	end-on: −1.09	distal		
anatase TiO_2 (101)	PBE, GGA+U	/	−0.18	/	N_2 adsorption energies, charge density difference	[93]
OV-anatase TiO_2 (101)		/	−0.62	/		
$Ti_3C_2O_2$		/	−0.34	/		
OV-$Ti_3C_2O_2$		/	−0.38	/		
TiO_2 (101)	PBE+Grimme-D2	/	−0.25	/	[Bader charge, N_2 adsorption energies, N_2 bond prolongation, free energy profiles	[94]
OV-TiO_2 (101)		/	−0.47	distal-alternating		
F-capped OV-TiO_2	GGA-PBE	/	−0.29	/	N_2 adsorption energy, adsorption energies of intermediates, reaction mechanism	[95]
F-OV-TiO_2 (101)		/	−0.31	/		
anatase TiO_2 (101)		/	−0.62	/		
Fe-TiO_2 (101)	PBE+U (3 eV for Ti)	/	/	enzymatic	N_2 adsorption energies, N_2 bond prolongation, reaction mechanism	[56]
Fe-doped TiO_2 (101)		/	/	enzymatic		
OV-Fe-doped TiO_2 (101)		/	side-on (Ti active site): −1.70, side-on (Fe active site): −1.47, end-on (Ti active site): −1.03, end-on (Fe active site): −1.02			

Table 3. continued

Catalyst	Functional	Molecular Dynamics	Adsorption energy [eV]	Mechanism	Calculated properties	References
pristine TiO$_2$	GGA-PBE, DFT+U	/	−0.17	N$_2$, NNH	band gap, DOS, electron density diagram, adsorption energies, free energy diagram	[53]
OV-doped TiO$_2$		/	−0.25	N$_2$, NNH	/	
Cu-doped TiO$_2$ with OV - TiO$_2$-OV-strain		/	−0.37	N$_2$, NNH, NNH$_2$ (distal)		
(TiO$_2$)$_{3, 6, and 12}$ clusters	GGA-PBE, D3	/	end-on (D3): (TiO$_2$)$_3$: −0.55, (TiO$_2$)$_6$: −0.47, (TiO$_2$)$_{12}$: −0.38	/	Bader charge, charge density difference, adsorption, N$_2$ bond prolongation	[57]
Ru-(TiO$_2$)$_{3, 6, and 12}$ clusters			end-on (D3): Ru-(TiO$_2$)$_3$: −1.34, Ru-(TiO$_2$)$_6$: −1.22, Ru-(TiO$_2$)$_{12}$: −0.39			
rutile TiO$_2$ (110)	BEEF-vdW	/	/	/	surface coverage probabilities, N$_2$ binding free energy (relative to the carbon substitution slab)	[97]
carbon-TiO$_2$ (110)		/	−1.89	distal		
TiO$_2$	/	/	−0.25	/	PDOS, N$_2$ adsorption, Bader charge, density difference, reaction mechanism	[55]
Ni-TiO$_2$	PBE, DFT+U (4.5 for Ti 3d), DFT−D3	/	−0.53	distal		
MXene		/	−3.18	/	N$_2$ and NH$_3$ adsorption energies, N$_2$ bond prolongation, free energy profiles	[96]
TiO$_2$ (101)		/	−0.36	/		
TiO$_2$/Co		/	−0.86	/		
TiO$_2$/Fe		/	−1.34	/		
TiO$_2$/Ni		/	−0.38	/		
TiO$_2$/Pt		/	−0.34	/		
TiO$_2$ (101) anatase	GGA-PBE, DFT−D2	/	0.17	/	N$_2$ adsorption energies, bond prolongation	[141]
OV-TiO$_2$(101)		/	0.342	/		
Ti$_3$C$_2$ MXene		/	2.731	/		
anatase OV-TiO$_2$ (101)	GGA-PBE, DFT−D3	/	/	/	band gap, DOS, PDOS, H binding energy, N$_2$ adsorption energies, N$_2$ bond prolongation, mechanism	[81]
Au$_4$Ru$_2$		/	/			
Au$_4$Ru$_2$/OV-TiO$_2$ (101)		/	end-on: −0.07, side-on: −1.33	distal, alternating, enzymatic		
Au$_4$Ru$_2$(SCH$_3$)$_8$(P(CH$_3$)$_3$)$_2$/TiO$_2$		/	/	/		
BaTiO$_3$	PBE	/	side-on: −4.60	distal	N$_2$ adsorption energy, N$_2$ bond prolongation, charge density difference, free energy profiles	[98]

Table 3. continued

Catalyst	Functional	Molecular Dynamics	Adsorption energy [eV]	Mechanism	Calculated properties	References
rutile TiO$_2$ (110)	GGA-PBE	/	/	associative	(Electron density, adsorption energies), free energy diagram	[142]
amorphous TiO$_2$ on rutile TiO$_2$ (110)		/	/	associative alternating		
pristine g-C$_3$N$_4$	PW91, DFT–D, HSE06	/	/	/	band structures, absorption spectra, electron transitions (HSE06), Fermi level, electron density difference, Hirshfeld charge, DOS, ELF (electron localization function), formation energies of NV-defective catalyst, adsorption, mechanism, free energy diagrams, HER	[59]
planar NV (central)-g-C$_3$N$_4$		/	/	distal, alternating, enzymatic		
planar NV(2-fold coordinated)-g-C$_3$N$_4$		/	/	/		
corrugated NV(central)-g-C$_3$N$_4$		/	/	alternating, enzymatic		
corrugated NV(2-fold coordinated)-g-C$_3$N$_4$		/	side-on: −2.56	alternating + distal, enzymatic		
NV-C$_3$N$_4$	/	/	−1.72 (−166.2 kJ/mol)	/	N$_2$ adsorption, N$_2$ bond prolongation	[99]
NV-g-C$_3$N$_4$	/	/	NV1:-1.72 (−166.2 kJ/mol) NV2: −0.02 (−2.4 kJ/mol)	/	N$_2$ adsorption, N$_2$ bond prolongation	[100]
g-C$_3$N$_4$ - NV (bulk)	/	/	/	/	N$_2$ bond prolongation	[101]
g-C$_3$N$_4$ - NV (001)	/	/	/	/		
g-C$_3$N$_4$	Wb97x-d/6-31G(d)* functional and basis set	/	position A: 0.03 Ha, position B: 0.022 Ha, position C: 0.017 Ha	alternating	N$_2$ adsorption energies, Gibbs free energies of N$_2$ fixation over both photocatalysts	[102]
V-rich g-C$_3$N$_4$		/	position A: 0.09 Ha, position B: 0.05 Ha, position C: 0.02 Ha	alternating		
VN-g-C$_3$N$_4$	GGA-PW91, OBS for DFT–D corrections	/	chemisorption: −3.52	/	N$_2$ adsorption energies, charge density difference	[103]
VN–S–g-C$_3$N$_4$		/	chemisorption: −4.54	/		
sulfur doped g-C$_3$N$_4$ (bulk SCNN)	GGA–D	AIMD, NVR, Nose-Hoover	−0.335	/	N$_2$ adsorption energies, charge density difference	[46]
CV-SCNN		/	CV active site: −0.665	/	/	
VN-g-C$_3$N$_4$	GGA-PW91, OBS for DFT–D corrections	/	−3.52	/	charge density difference, N$_2$ adsorption energies, charge density difference	[104]

ChemSusChem

Review
doi.org/10.1002/cssc.202301730

Chemistry
Europe
European Chemical
Societies Publishing

Table 3. continued

Catalyst	Functional	Molecular Dynamics	Adsorption energy [eV]	Mechanism	Calculated properties	References
VN–P-g-C$_3$N$_4$	/	/	−4.72	/	N_2 adsorption energies, N_2 bond prolongation, charge density difference	[60]
g-C$_3$N$_4$	/	/	−1.587	/		
Fe-doped g-C$_3$N$_4$	/	/	−1.911	/	DOS, N_2 adsorption energies, charge density difference, Mulliken charge	[61]
pristine g-C$_3$N$_4$	/	/	physisorption −14.6 kJ/mol	/		
Fe-g-C$_3$N$_4$		/	chemisorption −134.8 kJ/mol			
g-C$_3$N$_4$	GGA-PBE	/	physisorption: −0.26	/	N_2 adsorption energies, mechanism of HER	[105]
EDTA-g-C$_3$N$_4$		/	physisorption: −0.29	/		
Fe-EDTA g-C$_3$N$_4$		/	chemisorption: −0.99	/		
g-C$_3$N$_4$	GGA-PBE, DFT–D3	/	end-on: physical	/	N_2 adsorption energies, N_2 bond prolongation, energy barrier	[106]
Mo single atom-g-C$_3$N$_4$		/	end-on: chemical: −1.31 for N_2 and −0.39 for water	distal, alternating		
g-C$_3$N$_4$	GGA-PW91	/	−6.6 kJ/mol	/	DOS, N_2 adsorption, Hirshfeld charges, charge density difference, N_2 bond prolongation	[63]
Co-doped g-C$_3$N$_4$		/	−156.5 kJ/mol	non-dissociative mechanism		
pristine g-C$_3$N$_4$	GGA-PW91	/	−0.162	/	HOMO-LUMO, DOS, N_2 adsorption energies, N_2 bond prolongation, Mulliken charges, charge density difference	[62]
Ms-Cu$^+$-doped g-C$_3$N$_4$		/	−1.196	/		
K and –CN≡N g-C$_3$N$_4$	PBE–D3	/	CN≡N active site: −1.72	alternating	N_2 adsorption energies, charge transfer, reaction mechanism	[64]
g-C$_3$N$_4$ (CN)	GGA-PBE	/	−0.0299	/	N_2 adsorption energy, N_2 bond prolongation, Mulliken charge analysis, electron transfer-mechanism	[108]
ultrathin NV-g-CN (UCNx)		/	−0.1003	/		
BNUCNx		/	B1: −0.214, B2: −0.8063	/		
Ru/E-g- C$_3$N$_4$	PBE-GGA, DFT+U	/	side-on on Ru site: −2.18	dissociative, associative	CINEB for TS and barriers, Ru adsorption energies, N_2 adsorption energies, work functions, reaction mechanism, energy barriers	[107]
Ru/B-g-C$_3$N$_4$		/	end-on on Ru site: −1.31	dissociative, associative		
11 transition metals, M$_4$@B$_{36}$N$_{36}$	DFT–D3, HSE06	AIMD: 300 K in water	−0.01 to 0.89 (for M = Sc, Ti, V, Cr, Y, Zr, Mo, W)	enzymatic (on Mo$_4$@B$_{36}$N$_{36}$)	AIMD, Bader charge, HOMO-LUMO energies, average bond prolongation, M$_4$@B$_{36}$N$_{36}$ adsorption energies, N_2 adsorption, differential charge density differences, mechanism (Gibbs free energy diagrams), onset potentials)	[109]

Table 3. continued

Catalyst	Functional	Molecular Dynamics	Adsorption energy [eV]	Mechanism	Calculated properties	References
GaN	GGA-PBE, optB86 exchange functional	/	physical adsorption	/	N_2 adsorption energies, charge density difference, Bader charge (electron transfer), N_2 bond prolongation	[110]
NV-GaN (nitrogen vacancies)		/	chemical adsorption	/		
pristine C_2N	GGA-PBE functional, Grimmes's DFT–D2	AIMD: 300, 500, 800 K	/	/	optical absorption spectrum, band structures, AIMD, phonon dispersion spectrum, N_2 adsorption, N_2 bond elongation, reaction mechanism	[85]
B/C_2N		/	end-on: −1.44, side-on: −0.58	distal, alternating, enzymatic		
BiOCl	GGA-PBE, DFT–D3, HSE06 (electronic)	/	/	/	NAMD, band structures, optical absorption spectra, Bader charge, N_2 adsorption energies, HER	[65]
BiOBr		/	/	/		
BiOI		/	/	/		
Mo-BiOCl		NAMD: 300 K	different dopants: average, end-on: −1.42 to 0.25, Mo-BiOCl: −1.42	distal		
Mo-BiOCl/BiOBr heterojunction		NAMD: 300 K	/	/		
OV-BiOCl (001)	GGA-PBE	/	/	/	N_2 bond prolongation	[111]
pristine BiOCl (001)	GGA-PBE, DFT+U	/	/	/	N_2 adsorption energies, N_2 bond prolongation, charge density difference, Bader charge, free energy diagram (mechanism)	[112]
pristine BiOCl (010)		/	/	/		
OV-BiOCl (001)		/	chemisorption	distal		
OV-BiOCl (010)		/	chemisorption (by 0.42 eV (9.67 kcal/mol) more stable than OV-BiOCl (001))	alternating		
pristine BiOBr (001)	GGA-PBE	/	thermodynamically unfavorable (N_2 adsorption)	/	N_2 adsorption energies, mechanism, Gibbs free energies	[113]
OV-BiOBr (001)		/	/	distal		
OV-BiOBr(001)	PBE, DFT+U	/	side-on configuration, chemical adsorption	/	Bader charge, charge density difference, adsorption, N_2 bond prolongation	[114]
BiOBr (001)	GGA-PBE, PBEsol, DFT–D	/	end-on: 0.15	alternating	charge density difference, Hirshfeld charge analysis, N_2 adsorption energies, O_2 and H_2O adsorptions, reaction mechanism	[86]
OV–O-ter+H BiOBr (001)		/	end-on: −1.90, side-on1: −1.34, side2: −1.86, bridge-on:-1.32	distal		

Table 3. continued

Catalyst	Functional	Molecular Dynamics	Adsorption energy [eV]	Mechanism	Calculated properties	References
pristine BiOBr	GGA-PBE	/	/	/	formation energy of OV in Fe-BiOBr, charge density map	[115]
Fe-BiOBr+OV		/	/	/		
pristine BiOBr	DFT–D3, DFT +U (U=3.3, 8.6 and 3.4 eV for Fe, Mo and Ni)	/	−0.12	/	band structure, CBM, VBM postions, DOS, PDOS, N_2 adsorption energies	[66]
OV-BiOBr		/	−0.14	/		
Fe-BiOBr		/	−0.29	/		
Mo-BiOBr		/	M-> 0.14	/		
Ni-BiOBr		/	−0.12	/		
Fe-OV-BiOBr		/	−0.32	/		
Mo-OV-BiOBr		/	−0.26	/		
Ni-OV-BiOBr		/	−0.45	/		
Bi_3O_4Br	GGA-PBE, DFT +U	/	−0.087	/	DOS for SUC BiOBr; 002 facet the most exposed one, N_2 adsorption energies	[67]
SUC Bi_3O_4Br		/	−0.241	/		
pristine Bi_5O_7Br	GGA-PBE	/	−0.008	distal	N_2 adsorption energies, adsorption energies of intermediates, energy barrier, reaction mechanism	[116]
OV-Bi_5O_7Br		/	−0.017	distal		
Bi_5O_7Br+O atom		/	−0.001	distal		
$Bi_{12}O_{17}Br2$	GGA-PBE	/	−0.008	distal	N_2 adsorption energies	[117]
OV-$Bi_{12}O_{17}Br2$		/	−0.017	distal		
$Bi_4O_5Br_2$ (001)	GGA-PBE	/	0.03	alternating	N_2 adsorption energies, water dissociation energy	[68]
BrV-$Bi_4O_5Br_2$ (001)		/	−0.03	alternating		
Bi_2MoO_6	GGA-PBE	/	−0.83	alternating	N_2 adsorption energies, reaction mechanism	[143]
Gd-doped Bi_2MoO_6		/	−1.22	alternating	/	
beta-Sb(001)	PBE–D3, PBE-BJ (Becke-Johnson)	/	/	/	first hydrogenation in mechanism, binding free energy of first hydrogenation	[144]
beta-Sb(100)		/	/	/		
Sb_2O_3 (001)		/	/	/		
Sb(001)-SB vacancy		/	/	/		
Sb(100)-Sb vacancy		/	/	/		
Sb_2O_3 (001)-O vacancy		/	/	/		

Table 3. continued

Catalyst	Functional	Molecular Dynamics	Adsorption energy [eV]	Mechanism	Calculated properties	References
Bi$_3$FeMo$_2$O$_{12}$ (150)	GGA-PBE	/	/	associative, dissociative	reaction mechanism	[145]
(Bi$_x$M$_y$)$_2$MoO$_6$, m=Fe, La, Yb; Bi	GGA-PBE	/	/	dissociative for M=Fe, La, Yb	reaction mechanism	[146]
MoO$_3$ (001) and (100)	PBE+U (2.0 eV) for Mulliken and DFT–D2 for N$_2$ activation	/	/	/	DOS, Bader charge, Mulliken charge, binding energies (Mo—O), N$_2$ bond	[69]
OV-MoO$_3$		/	/	/		
WO$_3$	GGA-PBE	/	−0.28	alternating	N$_2$ adsorption energies, charge density difference, reaction mechanism	[118]
Fe-doped WO$_3$		/	−0.59	alternating		
W$_{18}$O$_{49}$ (001)	GGA-PBE	/	−1.65	/	charge density difference, N$_2$ adsorption energies, reaction mechanism	[119]
Mo-doped W$_{18}$O$_{49}$		/	−2.48	enzymatic		
β-Ga$_2$O$_2$ (111) facet	GGA-PBE	/	−0.975	alternating	N$_2$ adsorption energies, N$_2$ bond prolongation, reaction mechanism	[120]
Sb$_2$O$_3$	GGA-PBE	/	−0.35	/	N$_2$ adsorption energies, charge density difference, Bader charge	[71]
W$_{18}$O$_{49}$		/	−0.45	/		
Sb$_2$O$_3$/W$_{18}$O$_{49}$		/	−1.08	distal		
MoO$_{3-x}$	GGA-PBE+U (U=6.3 eV)	/	0.43	enzymatic	DOS, N$_2$ adsorption energies, charge density difference, Mullikan charge analysis, reaction mechanism	[73]
La-MoO$_{3-x}$		/	side-on: −1.08	enzymatic		
OV-ZnO$_{1-x}$ (100)	GGA-PBE, HSE06	/	1.37	/	N$_2$ adsorption energies, N$_2$ bond prolongation, Bader charge analysis	[121]
Ti-OV-ZnO$_{1-x}$ (100)		/	−1.08	/		
OV-ZnO$_{1-x}$ (002)		/	−0.09	/		
Ti-OV-ZnO$_{1-x}$ (002)		/	−0.47	/		
Ti-OV-ZnO$_{1-x}$ (Zn terminated) (002)		/	−0.91	/		
W$_{18}$O$_{49}$	GGA-PBE	/	−0.35	/	N$_2$ adsorption energy, N$_2$ bond prolongation	[72]
Fe/W$_{18}$O$_{49}$		/	/	/		
P-Fe/W$_{18}$O$_{49}$		/	−0.91	/		
ZnCr	GGA-PBE, DFT+U	/	/	/	Band gaps, N$_2$ adsorption energies, energy barrier for RDS, formation energy of OV, an energy barrier for the first hydrogenation	[76]

Table 3. continued

Catalyst	Functional	Molecular Dynamics	Adsorption energy [eV]	Mechanism	Calculated properties	References
ZnCr-LDH		/	(−0.45 eV when unsaturated Zn, −0.17 eV when saturated Zn)	N_2H		
ZnCr-LDH-OV		/	/	/		
ZnCr-OV		/	/	/		
CdS@LDHs-1	/	/	/	distal, alternating	reaction mechanism, energy barriers	[147]
CdS@LDHs-2		/	/	distal, alternating		
CdS@LDHs-3		/	/	distal, alternating		
pristine CuCr-LDH	DFT+U	/	−0.453	/	band structures, DOS, PDOS, N_2 adsorption energies	[75]
OV-CuCr-LDH		/	−0.81Li2022	/		
OV-CuCr-LDH		/	−0.81	/		
OV-CuCr-LDH + 1 % strain		/	−0.886	/		
ZnAl-LDH		/	−0.834	/		
OV-ZnAl-LDH		/	−1.016	/		
OV-ZnAl-LDH + 1 % strain		/	−1.08	/		
ZnAl-LDH	GGA-PBE, DFT + U	/	−0.03	/	Band gap, charge density difference, Bader charge, electronegativity difference, flat band potentials, N_2	[122]
OV-ZnAl-LDH-OV		/	−0.54	/		
OV−Cu-doped ZnAl-LDH		/	−0.94	/		
Fe-MIL-101	DFT+U	/	−0.48	N_2H, NNH_2	charge density difference, N_2 adsorption energy, Gibbs free energies for the first and second hydrogenation	[123]
Cr-MIL-101		/	−0.43	N_2H, NNH_2		
Gd-IHEP-7 (2D MOF)	GGA-PBE, UPBE−D3	/	end-on: −0.26	distal, alternating	TD-DFT, Mulliken charges, DOS, band structure, N_2 adsorption energies, CI NEB, reaction mechanism	[78]
Gd-IHEP-8 (3D MOF)		/	end-on: −0.29	distal, alternating		
Gd-IHEP-7 ligand gr replaced with CH_3		/	/	/		
Gd-IHEP-8 ligand gr replaced with CH_3		/	/	/		
Al-MOF	GGA-PBE−D3	/	/	/	N_2 adsorption energies, reaction mechanism	[124]
Fe−Al-MOF		/	end-on: ~ −0.50	distal, alternating		
MoS_2	GGA-PBE, D3 Grimme; DOS: HSE06	NVT MD, room T, water medium	/	/	DOS, Bader charge, Fe-MoS_2 binding energy, NBO, MD, Gibbs free energies	[49]

Table 3. continued

Catalyst	Functional	Molecular Dynamics	Adsorption energy [eV]	Mechanism	Calculated properties	References
Fe-MoS$_2$		/	−0.67 (Gibbs free energy)	distal	N$_2$ adsorption energies, N$_2$ bond prolongation	[125]
CdS	/	/	−0.033 (−3.2) kJ/mol chemisorption	/		
SV-CdS		/	−1.31 (−126.5 kJ/mol physisorption	/		
FeMoS-FeS-SnS	TPSSh functional	/	/	/	binding energies, N$_2$ bond prolongation	[126]
BPNS/CdS (0001) facet	GGA-PBE	/	−0.11	distal	charge density difference, N$_2$ adsorption energy, reaction mechanism	[127]
CdS (002)	GGA-PBE	/	1.16	/	N$_2$ adsorption energies, charge density difference	[128]
NiS (211)		/	−0.26	/		
Ni-doped CdS		/	−0.55	/		
Ru(001)	GGA-PBE, DFT–D	/	end-on: −0.83	/	N$_2$ adsorption, charge density difference, reaction mechanism	[22]
CoS		/	end-on: −0.58	/		
CoS$_x$(101)		/	end-on on SV: −0.98	/		
CoS$_x$(101)/Ru(001)		/	side-on: −1.01	enzymatic		
WS$_2$ monolayer	GGA-PBE	/	/	/	dopant formation energies, Hirshfeld charges, charge transfer (TM atom to SV), N$_2$ adsorption energies, N$_2$ bond prolongation, energy evolution profiles of N$_2$ adsorption, reaction mechanism, reaction barrier, S-vacancy formation	[129]
SV-WS$_2$		/	−0.04	/		
doped WS$_2$-SV (Ni-doped was further investigated)		/	end-on: −0.92, side-on: −0.69	distal, alternating		
MoS$_2$	GGA-PBE	/	basal plane: 1.07, S edge: 0.12, Mo edge: −0.47	first hydrogenation	N$_2$ adsorption energies, N$_2$ bond prolongation, reaction mechanism	[130]
Mn-MoS$_2$-SV		/	−0.2	distal		
Mn-MoS$_2$-2SV		/	−0.44	alternating		
SV-1T MoS$_2$/CsS composite	/	/	~−2.2 (Gibbs free energy)	distal, alternating	Gibbs free energies	[148]
Zn$_3$In$_2$S$_6$ (S-TA)	GGA-PBE	/	/	alternating	band gap, DOS, PDOS, reaction mechanism	[79]
ZN-defective Zn$_3$In$_2$S$_6$ (S-TAA)		/	/	alternating		
Ti$_{32}$O$_{52}$S$_8$	GGA-PBE, DFT–D3, HSE06 for bandgap	/	−0.76 – −2.1	/	band structures, N$_2$ adsorption energies	[80]
Ti$_{32}$O$_{61}$S$_2$		/	/	/		

Table 3. continued

Catalyst	Functional	Molecular Dynamics	Adsorption energy [eV]	Mechanism	Calculated properties	References
$BiVO_2/ZnIn_2S_4$ Z-scheme heterojunction	GGA-PBE	/	In site: −0.42, Zn site: −0.35, S site: −0.35	/	work functions, N_2 adsorption energies	[74]
SV-$BiVO_2/ZnIn_2S_4$ Z-scheme heterojunction		/	In site: −0.41, Zn site: −0.44, S site: −0.41, SV: −0.5	/		
Pt-SACs/CTF	GGA-PBE, DFT–D3 for AIMD	AIMD at 300 K	side-on: −0.97	distal, alternating	AIMD, Bader charge, charge density difference, N_2 adsorption energy, binding energies, Gibbs free energy of Pt incorporated into SACs/CTF	[47]
O_4/C	GGA-PBE	/	−0.12	/	N_2 adsorption energies, reaction mechanism, H adsorption energy	[131]
Fe_1O_4/C			end-on: −1.59, side-on: −1.46	hybrid distal, alternating pathway		
Fe_1O_4/C-PPH_3/NaI		/	−0.17	/		
Ti_3C_2 (001)	GGA-PBE	/		/	N_2 adsorption energy, charge density difference, N_2 bond prolongation	[132]
PaI)	GGA-PBE+U	/	end-on: −3.16; −2.75, side-on: −5.20	/	band gap, DOS, work functions, electrostatic potentials	[82]
Fe_2O_3		/	/	/		
30% Fe-PaI		/	/	/		
black phosphorene (BP)	GGA-PBE, HSE06	ab initio non-adiabatic MD: 500 K	0.25–1.86	/	*ab initio* non-adiabatic MD, formation energies of vacancy defects, band gaps, band edges, DOS, PDOS, N_2 adsorption energies, bond prolongation	[83]
DV-BP		/	1.92	/		
blue phosphorene (BuP)		/	0.25–1.86	/		
DV-BuP		/	1.28	/		
DV-BP and DV-BuP + ione pair		/	0.15–0.66	/		
BMO	GGA-PBE, DFT+U	/	−1.91	/	N_2 adsorption energies, N_2 bond prolongation, reaction mechanism, electrostatic potentials	[133]
OV-BMO (010)		/	−3.95	distal		
c-PAN (cyclized polyacrylonitirle)/ Bi_2WO_6	GGA-PBE	/	/	/	N_2 bond prolongation, electron transfer	[134]
$LaFeO_3$ (121)	GGA-PBE	/	/	/	N_2 bond prolongation	[135]
$FeCo_2O_4$ (311)	DFT+D3+U	MD	−0.78	alternating, distal	MD, PDOS, charge density difference, N_2 adsorption energy, reaction mechanism	[136]
CdS (002)/LDH(003/012) heterojunction	GGA-PBE	/	/	alternating, distal	work functions, reaction mechanism	[147]
HNb_3O_8	GGA-PBE	/	/	/	N_2 bond prolongation, charge density difference	[137]
$HNbO_3$		/	/	/		
B-OV-$HNbO_3$		/	/	/		

Table 3. continued

Catalyst	Functional	Molecular Dynamics	Adsorption energy [eV]	Mechanism	Calculated properties	References
OV-InVO$_4$	DFT–D3	/	V^{4+} active site: −0.96, OV active site: −0.54, In active site: 0.03	distal, alternating	N$_2$ adsorption energy, reaction mechanism	[138]
ZnCr	GGA-PBE, DFT+U	/	/	/	Band gaps, N$_2$ adsorption energies, energy barrier for RDS, formation energy of OV	[76]
ZnCr-LDH		/	(−0.45 eV when unsaturated Zn, −0.17 eV when saturated Zn)	/	/	
ZnCr-LDH-OV		/	/	/	/	
ZnCr-OV		/	/	/	/	
Ce-CUS (loaded on MOF-76 Ce)	DFT+U	/	/	/	DOS, charge transfer	[77]
Ru-SA/ H$_x$MoO$_{3-y}$	GGA-PBE+U	/	Mo^{n+} active site: 0.4 eV lower than on Ru SA active site	/	PDOS, Gibbs free energies of OV formation, N$_2$ adsorption energies, formation of some intermediates	[70]
1 OV - Ru-SA/ H$_x$MoO$_{3-y}$		/	−0.104	/		
2 OVs - Ru-SA/ H$_x$MoO$_{3-y}$		/	−0.766	H$_2$-NH-NH, H$_2$-NH$_2$, H$_2$-NH$_2$-H$_2$,NH$_3$,NH$_3$ intermediates		
Bi$_3$FeMo$_2$O$_{12}$	GGA-PBE	/	/	associative, dissociative	reaction mechanism	[145]
OV-Bi$_3$FeMo$_2$O$_{12}$		/	/	associative, dissociative		

ChemSusChem

Review
doi.org/10.1002/cssc.202301730

Chemistry Europe
European Chemical
Societies Publishing

Sun et al.[81] examined compared OV-TiO$_2$ (101) and Ag$_4$Ru$_2$/ OV-TiO$_2$K (101). They investigated the distal, alternating and enzymatic pathways and found that the formation of *NNH inetrmediate with a kinetic barrier of 1.36 eV is the rate-limiting step in the distal and alternating pathways with N$_2$ adsorbed on the Ru active site via the end-on coordination. All other steps were reported to be exothermic with low barriers (below 0.97 eV). The enzymatic pathway proved to be less favourable than the distal and alternating mechanisms. In addition, the authors also investigated the photolysis of water as a proton source and found a kinetic barriers of 0.09 eV and 0.02 eV for the dissociation of water on the surface and subsurface of OV-defective TiO$_2$ (101), respectively. Rutile TiO$_2$ (110) and amorphous TiO$_2$ loaded onto the surface of rutile TiO$_2$ (110) were investigated at the PBE level by Li et al.,[142] who proposed the associative mechanism and found lower free energies of intermediates on TiO$_2$/a-TiO$_2$ than on the pristine catalyst. It is suggested that a-TiO$_2$ facilitates nitrogen reduction because it is mainly composed of TiO$_4$ units, contains more defects and thus stabilizes the intermediates formed during the successive hydrogenation steps.

Oxygen vacancies and metal doping of TiO$_2$ facilitate nitrogen fixation and subsequent hydrogenation steps to synthesize ammonia by reducing the free energy barriers. Most commonly, the first hydrogenation step is determined to be the rate-determining one, and the mechanism proceeds via the alternating or distal pathways.

4.3.2. Pristine and Modified g-C$_3$N$_4$

Ren et al.[59] studied the distal, alternating and enzymatic mechanism at the PW91+D level over planar and corrugated NV-g-C$_3$N$_4$, identifying the latter as more favourable with lower onset potentials. The alternating mechanism proved predominating with the second hydrogenation to N$_2$H$_2$* as the rate-determining step with a ΔG of 1.32 eV. On the other hand, Shi et al.[102] found the first hydrogenation on pristine and V-rich g-C$_3$N$_4$ at the wB97X–D level as rate-determining with ΔG of 0.30 and 0.22 eV, respectively. The authors noticed that successive reaction steps were all negative in the alternating pathway but further lowered over the defective catalyst.

The role of different dopant atoms was extensively explored.[64,106,107,109] Guo et al.[106] proposed the distal and alternating pathways over Mo-immobilized g-C$_3$N$_4$ and concluded that both mechanisms are feasible, with the first hydrogenation being the rate-determining step (a barrier of 0.81 eV). Liu et al.[64] studied pristine, Bi-defected and dual defected (K and−C≡N) g-C$_3$N$_4$. Studying the proposed associative alternating mechanism over pristine g-CN, g-CN−K, g-CN-C≡N, CN−K-C−N(K), and CN−K-C00N(−C≡N), it was found that the reaction is most thermodynamically feasible over CN−K-C≡N(−C≡N). The formation of a *NHNH intermediate was the rate-determining step with a barrier of 1.29 eV. Liu et al.[107] used the PBE+U approach over Ru$_{11}$/E-g-C$_3$N$_4$ and Ru$_{11}$/B-g-C$_3$N$_4$ and found the associative pathway over Ru$_{11}$/E-g-C$_3$N$_4$ and the dissociative mechanism over Ru$_{11}$/B-g-C$_3$N$_4$. For both photocatalysts, the rate-determining step was the transformation of the end-on to the side-on adsorption configuration of N$_2$ with ΔG of 1.13 eV (over Ru$_{11}$/E-g-C$_3$N$_4$) or 0.71 eV (over Ru$_{11}$/B-g-C$_3$N$_4$).

Yang et al.[109] studied M$_4$@B$_{36}$N$_{36}$ (with metals (M) being Sc, Ti, V, Cr, Y, Zr, Nb, Mo, Hf, Ta, and W). Due to the side-on nitrogen adsorption, only the enzymatic pathway was explored. The Gibbs free energy of NRR over Mo$_4$@B$_{36}$N$_{36}$ showed that the rate-determining step is the hydrogenation of *NH$_2$ to *NH$_3$ with a ΔG 0.19 eV. Catalysts involving other metals exhibited higher barriers for the corresponding steps. Therefore, only Mo$_4$@B$_{36}$N$_{36}$ was used for simulations with implicit solvation with a dielectric constant of 80, which showed a further lowering of the energy barrier to 0.04 eV.

Bhattacharyya et al.[85] studied B/C$_2$N at the PBE+D2 level. Of all three associative mechanisms, the enzymatic pathway proved to be the most promising with the second hydrogenation as the potential-determining step with a barrier of 0.18 eV (for the distal and alternating pathways, the values are 0.99 and 0.71 eV, respectively). While the HER reaction competes with NRR, H adsorption was calculated with the energy of −2.37 eV and hence NRR was ruled to be predominant.

Distal and alternating mechanisms are predominant over the g-C$_3$N$_4$ photocatalyst with the first or second hydrogenation as the rate determining step. Nitrogen vacancies or metal doping show similar energy barriers for the corresponding rate-determining step, indicating that both modifications improve the reduction compared to the pristine catalyst.

4.3.3. BiOX and BOC

Zhao et al.[65] also used the PBE−D3 approach on various transition metal-doped BiOX (X=Cl, Br). For the associative distal mechanism, the first ammonia formation was determined as the rate-limiting step with the ΔG between 0.06 and 1.21 eV for most doped BiOCl catalysts. Mo-doped BiOCl exhibited the lowest onset potential of −0.22 V, the highest activity and selectivity. Li et al.[112] studied the OV-BiOCl (001) and (010) proposed the distal pathway on the former, while on BiOCl (010) favoured the alternating pathway with the first hydrogenation as the slowest step. Liu et al.[86] also found the first hydrogenation step of N$_2$ on different atomistic terminations of BiOBr as the rate-determining step with ΔG of 0.89 and 0.82 eV for Bi−Br and OV−O-ter+H catalysts, respectively. Over OV−O-ter+H, the distal pathway was investigated due to the end-on adsorption configuration, while the alternating mechanism was confirmed for the reduction over the Bi−Br facet. On the latter, hydrazine formation was excluded due to a positive value of ΔG of 0.53 eV for hydrogen desorption.

Li et al.[116] explored the distal pathway over pristine Bi$_5$O$_7$Br, OV-Bi$_5$O$_7$Br and Bi$_5$O$_7$Br+O. The last hydrogenation from *N-NH$_2$ to *N-NH$_3$ proved to have the largest energy barrier and was therefore considered as the rate-determining step. The free energy values for this reaction step differed depending on the catalyst chosen: 3.213, 3.019 and 3.019 eV over Bi$_5$O$_7$Br+O, pristine Bi$_5$O$_7$Br and OV-Bi$_5$O$_7$Br, respectively. Among the three, Bi$_5$O$_7$Br-OV seemed most promising for NRR. DFT and AIMD simulations with implicit solvation were performed by Dong et al.[68] to study the formation of O and Br vacancies in Bi$_4$O$_5$Br$_2$ (001). Studying the alternating pathway, the first hydrogenation of N$_2$ was the rate-determining step with a barrier of 2.36 and 2.00 eV on pristine and Br−V- Bi$_4$O$_5$Br$_2$, respectively. Induced Br vacancies decreased the reaction energy and the thermody-

ChemSusChem

Review
doi.org/10.1002/cssc.202301730

Chemistry Europe
European Chemical
Societies Publishing

namic barriers. Similarly, Li *et al.*[116] and Gao *et al.*[117] also studied the distal pathway over bulk and ultrathin OV-$B_{12}O_{17}Br_2$ and found the hydrogenation of *N-NH$_2$ to *N-NH$_3$ as the rate-determining step. Ultrathin OV-$B_{12}O_{17}Br_2$ exhibited lower Gibbs free energies, indicating a favourable effect of Br vacancies.

4.3.4. Other Oxides

Studying the reaction mechanism over the $Sb_2O_3/W_{18}O_{49}$ heterojunction with PBE, Hui *et al.*[71] found that the distal pathway is most promising with desorption of the first ammonia molecule as the potential-determining step with the a barrier of 0.65 eV and the free energy of the activation of adsorbed nitrogen molecule of −0.35 eV. Li *et al.*[143] studied NRR over pristine and Gd-doped 2D Bi_2MoO_6 catalysts and showed that it proceeds via the alternating mechanism. Gd doping, and thus the formation of the Gd3+ redox center, resulted in reduced free energies of the overall NRR, while the hydrogenation of *NHNH$_2$ and the formations of both NH$_3$ molecules exhibited the largest Gibbs free energies.

Zhao *et al.*[144] used PBE−D3-BJ (Becke-Johnson) to investigate the free energies of the first hydrogenation of N$_2$ on Sb(001), SbV−Sb(001), Sb(100), SbV−Sb(100), Sb_2O_3 (001), and OV-Sb_2O_3 (001). The first hydrogenation of adsorbed nitrogen was most feasible over OV-Sb_2O_3 (001) with ΔG of 1.57 eV. ΔG over the Sb vacancies of Sb(001) and Sb(100) were slightly higher (1.66 and 1.94, respectively) but lower than those on the pristine catalysts.

Over pristine and La-anchored $MoO_{3−x}$, Liu *et al.*[73] found out that since N$_2$ adsorbs in the side-on configuration, the enzymatic pathway is preferred. Anchoring of a single La atom decreases the Gibbs free energies and promotes the reaction. Using PBE, Ren *et al.*[118] showed that NRR occurs via the alternating pathway on pristine and Fe-doped WO$_3$. The energy barrier for the first hydrogenation is 0.2 eV lower over Fe-WO$_3$.

4.3.5. Layered Double Hydroxides and Metal Organic Frameworks

Zhao *et al.*[76] studied the saturated and unsaturated Zn active sites of ZnCr-layered double hydroxide (LDH). The rate-determining step was found to be the cleavage of the N$_2$ triple bond with a barrier of 0.89 eV when N$_2$ was adsorbed on unsaturated Zn and 2.44 eV on saturated Zn active sites. Unsaturated Zn active sites can be easily formed when the photocatalyst contains Zn vacancies. Three promising heterojunctions of CdS@LDHs were studied by Zhang *et al.*,[147] who determined the first hydrogenation as the rate limiting step with barriers of 2.24, 1.69 and 1.38 eV for CdS@LDHs-1, CdS@LDHs-2 and CdS@LDHs-3, respectively. It was found that the solvated electrons provided by water participate in NRR, while the potential of water (−2.86 V vs NHE for $H_2O + e^- \rightarrow e_{aq}^-$) is lower than the potential required to produce ·H from H$^+$ and e$^-$ (−2.3 V vs NHE).

Different metal organic frameworks were studied by Li *et al.*,[123] Hu *et al.*[78] and Shang *et al.*[124] On MIL-101(Cr) and MIL-101(Fe), Li *et al.*[123] calculated the Gibbs free energies for the first (~1.75 and 1.3 eV on MIL-101(Cr) and MIL-101(Fe), respectively) and second hydrogenation (~1.1 and 0.9 eV on MIL-101(Cr) and MIL-101(Fe), respectively) and found that Fe is more efficient due to two extra electrons in the *d*-orbital. The mechanism of photocatalytic NRR at the surfaces of Gd-IHEP-7 and Gd-IHEP-8 was explored by Hu *et al.*,[78] who proposed the alternating and distal pathayy and found an endothermic first hydrogenation of N$_2$ on Gd-IHEP-7 by +0.25 eV and exothermic on Gd-IHEP-8 by −0.63 eV. The intermediates formed during the NRR over Gd-IHEP-8 have extra hydrogen bonds, resulting in lower free energies compared to Gd-IHEP-7. Studying Al-PMOF and Al-MOF (Fe), Shang *et al.*[124] examined the alternating and distal pathway over Al-MOF (Fe) due to a more favourable adsorption energy of N$_2$ compared to the pristine catalyst. In the alternating pathway, the first hydrogenation (0.54 eV) was the rate-determining step, while the distal pathway was excluded due to a high energy barrier of the first hydrogenation of N* (4.51 eV).

4.3.6. Sulfides

Azofra *et al.*[49] looked into N$_2$ reduction on Fe-deposited MoS$_2$, finding that after the first hydrogenation, Fe-NNH· is formed and converted into NNH$_2$ (ΔG=0.85 eV and ΔG=0.13 eV), suggesting the distal pathway. Shen *et al.*[127] suggested two possible reaction pathways for photocatalytic NRR on the surface of BPNSs/CdS. On edge P atoms, it proceeded via the alternating pathway, and via the distal pathway when on surface P active sites. Yuan *et al.*[22] propounded the enzymatic pathway on Ru(001)/CoS_x(101) since N$_2$ was adsorbed in the side-on configuration on the Ru−Co active site. When the first hydrogenation occurred on the Ru atom, the rate-limiting step was the formation of *NH-NH$_2$ with ΔG of 0.68 eV (from −0.87 eV for *NH-NH to −0.19 eV for *NH-NH$_2$). On the other hand, when N was first hydrogenated on the Co atom, ΔG for the formation of *NH-NH$_2$ was 1.14 eV (from −0.87 eV for *NH-NH to 0.27 eV for *NH$_2$-NH), indicating that Ru is more favorable for first hydrogenation compared to Co in the Ru−Co active site (Figure 8).

S-vacancy defective WS$_2$ monolayers with different transition metal single atoms on the surface were studied by Ma *et al.*,[129] winnowing out Ni as the most favorable for anchoring on SV-WS$_2$ as active sites for nitrogen chemisorption. Considering the associative and enzymatic pathways for photo-NRR, the dissociative and associative enzymatic mechanisms were ruled out based on Gibbs free energies in favour of the associative mechanism (distal or alternating) with the end-on adsorption. An alternating pathway proved to be the most favourable with the first hydrogenation of nitrogen as the rate-limiting step with ΔG of 0.86 eV. On the other hand, a distal pathway exhibited two endothermic ΔGs, namely the first and third hydrogenations with ΔG of +0.86 eV and +0.99 eV, respectively. Therefore, the distal pathway was excluded.
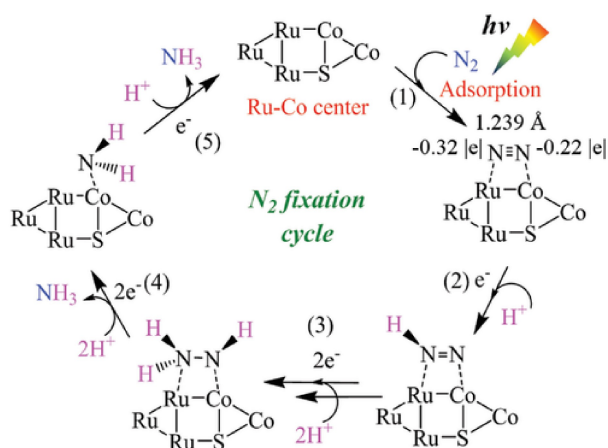
ChemSusChem

Review
doi.org/10.1002/cssc.202301730

Chemistry Europe
European Chemical
Societies Publishing

Figure 8. A reaction mechanism of NRR over Ru–Vs-CoS/CN. Reprinted with permission from [22].

Hu et al.[130] probed Mn-MoS$_{2-x}$ and Mn-MoS$_{2-x}$-2Sv, confirming the distal pathway on Mn-MoS$_{2-x}$ and alternating pathway on Mn-MoS$_{2-x}$-2Sv. The difference is due to a higher amount of the exposed Mo sites on Mn-MoS$_{2-x}$-2Sv, also resulting in a lower energy barrier of 0.87 eV compared to Mn-MoS$_{2-x}$-Sv (1.37 eV) and pristine catalyst (1.5 eV).

On the SV-1T-MoS$_2$/CdS composite, the associative alternating pathway was confirmed, since the second hydrogenation exhibited 0.4 eV lower free energy for the formation of the *NHNH intermediate compared to *NNH$_2$. Thereafter, successive hydrogenation steps occurred until the first and second ammonia molecules were formed and then desorbed with the energy barriers of ~0.11 and 2.97 eV, respectively.[148]

Han et al.[79] studied the reaction over ZnV-Zn$_3$In$_2$S$_6$, where Zn-vacancies as cationic defects were considered as active sites. End-on adsorption of N$_2$ and its activation was followed by the first hydrogenation by H$^+$ delivered from methanol, which was used as a hole sacrificial agent. The following intermediates may be formed are: NH–N*, NH-NH*, NH$_2$-NH*, NH$_2$-NH$_2$* and NH$_3$-NH$_2$*. It was found that Zn$_3$In$_2$S$_6$ increased nitrogen activation compared to untreated Zn$_3$In$_2$S$_6$.

4.3.7. Other Photocatalysts

Li et al.[47] proposed the distal and alternating mechanisms over the Pt-SACs/CTF catalyst and found the alternating mechanism thermodynamically more favorable with an energy barrier of 1.26 eV for the first hydrogenation (as shown in Figure 9). The distal pathway exhibited two endergonic steps (first and third hydrogenation of 1.26 eV and 1.54 eV, respectively), whereas in the alternating pathway only the first hydrogenation with the ΔG of 1.26 eV is endergonic. Therefore, the authors selected the alternating pathway as the most favorable for NRR.

Based on the adsorption results, Hou et al.[131] investigated the NRR via a hybrid distal to alternating pathway when N$_2$ was adsorbed on the Fe active sites of Fe$_1$O$_4$/C via an end-on configuration (Figure 10). The rate-limiting step of NRR via a hybrid distal to alternating pathway was the first hydrogenation of N$_2$ with a ΔG of 1.00 eV. The authors proposed an electron transfer in Fe$_1$O$_4$/C-PPh$_3$/NaI. Upon light illumination, the electrons in PPh$_3$/NaI are photogenerated and transferred to Fe atoms, which act as active sites for nitrogen adsorption. The latter radical, oxidizes water to oxygen and H radicals are formed.

Pei et al.[83] studied defective BP and BuP (black and blue phosphorene, respectively) in vacuum and in the self-consistent continuum solvation model with a relative permittivity of 78.4. The limiting steps were determined to be the protonation of *NH*NH$_2$ to *NH$_2$*NH$_2$ with an overpotential of 0.40 V and 0.67 V for DV-BP and DV-BuP, respectively. In defective BuP, the limiting step was protonation of *NH*NH (both, distal and enzymatic mechanisms) with ΔG of 0.84 eV. On the other hand, for SV-BP and BuP, NRR was found to proceed via the enzymatic mechanism, with the rate-determinin steps of 0.52 and 0.29 eV
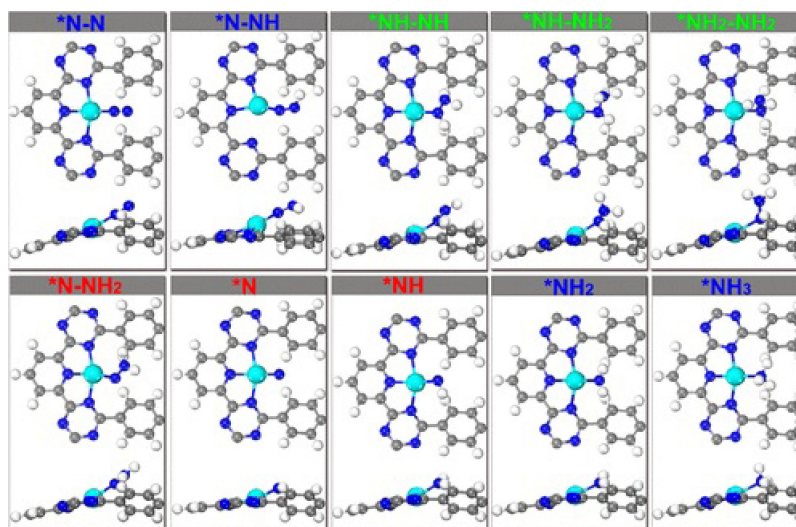

Figure 9. Intermediates formed during the distal and alternating pathways. Reprinted with permission from [47]. Copyright 2020 American Chemical Society.
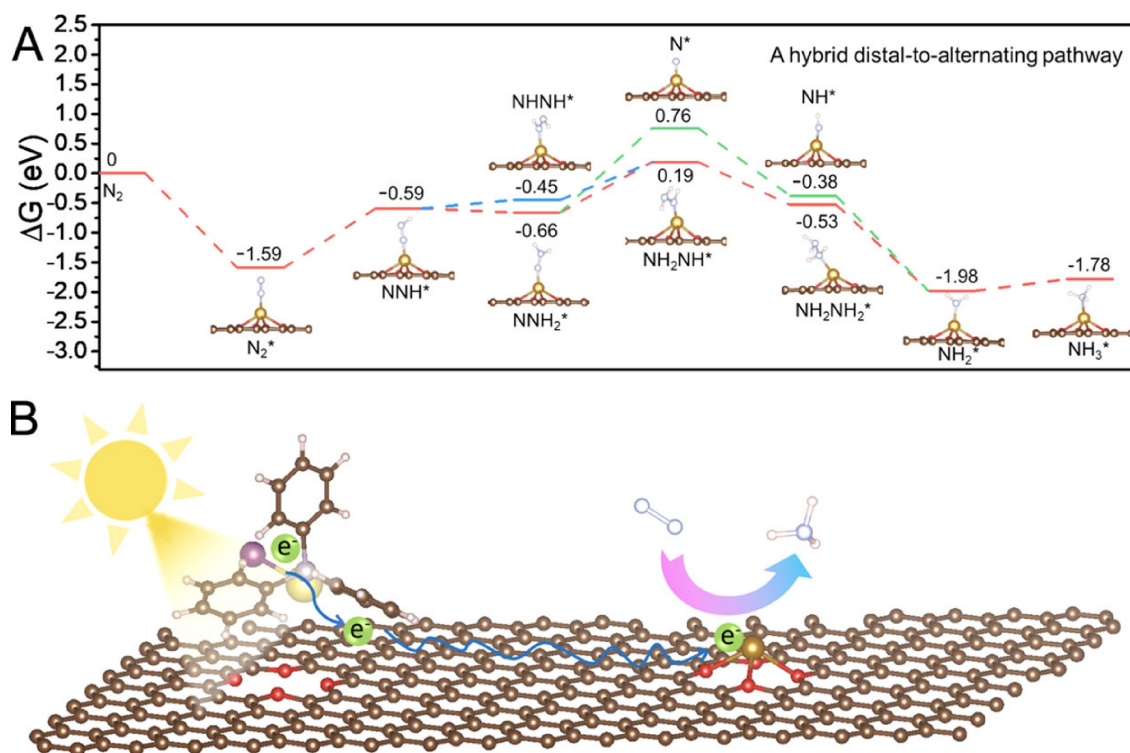
ChemSusChem

Review
doi.org/10.1002/cssc.202301730

Chemistry Europe
European Chemical
Societies Publishing

Figure 10. A) A hybrid pathway proposed for N_2 fixation over the Fe_1O_4/C catalyst. B) A shematic representation of photocatalytic NRR over the Fe_1O_4/C catalyst. Reprinted with permission from [131]. Copyright 2020 American Chemical Society.

being the protonations of *NN*H to *NH*NH and *NH to *NH$_2$, respectively. Furthermore, account for solvation resulted in lowering the limiting potentials to -0.20 V to -0.37 V compared to vacuum (-0.28 to -0.84 V). A competitive reaction (HER) was also studied and found to be more favorable for the evolution of H on phosphors with introduced SV defects.

Fe sites in $FeCo_2O_4(311)$ favoured the alternating pathway, as shown by lower Gibbs free energies and barriers, and higher Bader charge transfer between the Fe site and the corresponding successive intermediates during the reaction pathway, calculated at the PBE+D3+U level ($U_{Fe}=2.9$ and $U_{Co}=3.8$). In the distal pathway, the third hydrogenation proved to be the rate-determining step with a barrier of 0.99 eV, while in the alternating pathway only the first hydrogenation exhibited ΔG of 1.18 eV (both pathways share this step), indicating that the alternating pathway is more promising.[136] Zhang *et al.*[147] proposed the alternating and distal reaction pathway over the CdS (002)/LDH(003/012) heterojunction. Over CdS@LDHs-3, the alternating pathway was found to be more promising with the first hydrogenation step rate-determining with the relative energy for this step of 1.38 eV. The photocatalytic NRR was also investigated over pristine, boron-doped, and oxygen-vacancy modified HNb_3O_8 and $HNbO_3$ photocatalysts.[137] The distal pathway has lower barriers and the third hydrogenation (to NH$_3$) is the rate-determining step with a barrier of 0.67 eV over V-OV-$HNbO_3$ and 1.11 eV over OV-HNb_3O_8. On the latter catalyst, the alternating mechanism predominated. Pristine and modified HNb_3O_8 exhibited higher barriers and were therefore

not considered. Hence, boron doped V-OV-$HNbO_3$ with oxygen vacancies was the most promising catalyst.

Yao *et al.*[138] studied NRR over OV-$InVO_4$ at the PBE+D3 level and showed that the first hydrogenation is the rate determining step with a barrier of 0.88 eV for the pristine catalyst and 0.33 eV for OV-$InVO_4$. The OV-modified catalyst is more promising for efficient NRR due to a faster rate-determining step and lower Gibbs free energies along the reaction pathway. When dual active centers (Ru SA and Mo^{n+}) were added to H_xMoO_3, the formation energy of two oxygen vacancies was 0.956 eV lower in Ru/MoO_3 than in the pristine catalyst.[70] Hydrogen dissociation with synergistic successive hydrogenation steps formed two ammonia molecules over the Mo active site of Ru-SA/ H_xMoO_3 with two oxygen vacancies.

NRR was also studied by Liu *et al.*[145] on the surface of $Bi_3FeMo_2O_{12}$, investigating the associative and a dissociative pathways. They found that the rate-determining step on the pristine surface is the formation of 2NH_2* in the associative pathway and of 2 N* intermediates in the dissociative pathway. It was also observed that a small amount of OV enhances nitrogen activation as the stability of the N-OV-$Bi_3FeMo_2O_{12}$ is higher, while a higher amount of OV decreased the stability of the photocatalyst structure. This was also confirmed by hydrogen treatment at T>300 °C, where along with the OV formation the Mo atoms became unsaturated, forming Mo^{5+} active sites.

ChemSusChem

Review

doi.org/10.1002/cssc.202301730

Chemistry Europe
European Chemical
Societies Publishing

4.3.8. Relationship Between the Adsorption Configuration and Reaction Mechanism

As amply shown hitherto, the reaction mechanism of photo-catalytic NRR is intimately connected to the adsorption configuration of N_2. The end-on adsorption favours the distal or alternating associative mechanism, while the side-on adsorption prompts the enzymatic associative mechanism. The dissociative mechanisms are rarely considered as the activation and subsequent reaction steps occur preferably via the associative mechanisms. The first hydrogenation is most often the rate-determining step but this varies depending on the catalyst and modification. The hydrogen evolution reaction is sometimes studied as a competitive reaction to NRR.

4.4. Reaction Mechanism in the Excited State

Comparatively few studies have focused on the reaction mechanism in the excited state due to the computational cost and methodological complexity of such an approach. Among those, Martinez et al.[150] studied N_2 dissociation on Fe-doped Au(111) in the ground and excited state. For the former, they used the PBE–D3 functional and the embedded correlated wavefunction (ECW) within DFT to improve the ground state results and to obtain electronically excited state energies. The authors calculated the isosurface of the embedding potential of the $Au_{10}Fe$ cluster, the residual Bader charges, the vibrational frequencies of nitrogen bonds, the adsorption and adiabatic dissociation pathways. At the PBE–D3 level, they found that N_2 is adsorbed on the Fe active site in the end-on configuration with an energy of -0.61 eV (the corresponding Gibbs free energy is -0.07 eV at $T = 298$ K and $p = 1$ atm) and then rotated in the side-on configuration over a Fe–Au bridge site. An activation barrier of 3.80 eV was calculated for the latter dissociation. Initially, the spin multiplicity of N_2 changes from S_z 2 to 1 in the process, and ultimately to S_z 0 upn dissociation. The authors then used the density functional embedding theory and studied nitrogen dissociation on an $Au_{10}Fe$ cluster and found higher barriers predicted by emb-CASPT2 (4.63 eV) and emb-NEVPT2 (4.74 eV) compared to DFT–D3 calculations (3.80 eV). Moreover, the reaction energies for the ground state nitrogen dissociation also increased from 2.37 eV (DFT–D3) to 3.19 eV (emb-CASPT2) and 3.62 eV (emb-NEVPT2). Approximately one electron per dissociated nitrogen atom is transferred from the Fe active.

To probe the excited states, calculations using a plasmon-induced resonance energy transfer (RET) were performed and the lowest dissociation barrier of 1.33 eV was found at room temperature due to the availability of electronically excited states and crossing between them. Similarly, they studied the dissociation of nitrogen on a Mo active site of Mo-doped Au (111) surface[151] and found an even lower energy barrier of 0.77 eV (at the emb-NEVPT2 level) and ~3.5 eV in the ground state (PBE–D3). Absorption spectra of selected structures along the dissociation pathway, the corresponding electron density differences and the mechanism of the plasmon energy transfer

to the Mo active site were also calculated. Consistent with a previous study,[150] they found that electronic excitations lower the activation barriers. Photocatalytic nitrogen dissociation is more feasible on Fe–Au(111)[150] or Mo–Au(111)[151] than on pristine Au (111) (a barrier of 4.98 eV),[152] Fe (110) (a barrier of 1.11 eV),[153] flat[154] or stepped[155] Ru (0001) surfaces (1.90 eV and 0.78 eV, respectively), or Fe/Ru(0001) (0.74 eV).[153]

Martinez et al.[152] also explored N_2 dissociation over AuM (M =Mo, Co, Ni and Fe), where the plasmonic behavior of Au and the catalytic behavior of metal make to the forefront, where AuMo and AuFe alloys performed best. These decreased the dissociation energy of N_2 by 3.2 eV (AuFe) and 4.7 eV (AuMo) compared to Au(111). However, AuFe exhibited better stability, while the performance of AuMo was limited by its susceptibility to oxidation.

5. Kinetic Modelling

While ab initio calculations of the electronic structures reveal important information about the structure, properties and performance of catalysts, kinetic modelling captures the evolution of the system during the reaction. It allows us to simulate and quantify turnover frequencies, surface coverages, catalyst selectivity and activity. Using first-principles derived information on the reaction pathways, such as activation barriers, pre-exponential factors, or rate constants of elementary reaction steps, the exact mechanism and contribution of individual reactions can be followed. Mean-filed kinetic modelling assumes average coverages of the catalyst, while kinetic Monte Carlo can account for co-adsorption effects when lateral interactions are included.

Most of the reviewed studies use the kinetic parameters derived from experimental work to construct a kinetic model, which was effectively to experimental observables. They mostly focus on or electrocatalytic processes, while kinetic studies of photocatalytic NRR lag behind. They are rarely coupled with ab initio calculations and used lumped kinetics instead of individual elementary reaction steps. On the other hand, photocatalytic reduction of CO_2 has been treated with first-principles kinetic simulations extensively.[156–158] Regarding NRR, there is ample room for improvement in terms of kinetic modelling of photocatalytic reactions, especially when including excited states and the effects of irradiation of the reactor set-up.

Below, we list the kinetic modelling efforts of NRR.

5.1. First-Principles Based Kinetic Modelling

Christianson et al.[159] used their DFT calculations in a kinetic model coupled with MD simulations to describe photocatalytic nitrogen reduction by aqueous solvated electrons. The model also included H_2 production and solvated electrons, using the following reactions:

1. $N_2 + H \rightarrow N_2H$ (HAA – hydrogen atom addition)
2. $N_2 + e^- \rightarrow N_2^-$ (ET – electron transfer)

ChemSusChem

Review
doi.org/10.1002/cssc.202301730

Chemistry Europe
European Chemical
Societies Publishing

3. $N_2 + e^- + H_2O \rightarrow N_2H + OH^-$ (PCET – proton coupled electron transfer)

From firs principles, a rate constant of 930 $M^{-1}s^{-1}$ was calculated for the hydrogen atom addition reaction. The phase barrier and rate constant of the electron transfer were determined using Marcus theory and MD simulations to describe the solvent and N_2. The MD calculations were performed for 150 ps at 298 K in the NVT ensemble and the barrier to form N_2^- with solvated electrons was described with Marcus theory. In addition, the rate constant and barrier of PCET were calculated as a 2D extension of Marcus theory in a process coupled with protons and electrons. However, although the photocatalytic reaction was also performed experimentally, the kinetics were modeled in the absence of irradiation. The modelling revealed that NRR proceeds via HAA, followed by protonation and reduction of solvated electrons.

Gouveia et al.[160] coupled DFT calculations at the PBE + D3 level with a microkinetic model to study nitrogen fixation over a 2D inorganic MXene catalyst. First, nitrogen adsorption modes were determined on the M_2C and M_2N MXen (0001) surfaces (where M denotes Ti, Zr, Hf, V, Nb, Ta, Cr, Mo and W) to winnow out the most promising catalysts. The reaction mechanism was then studied over Nb_2C, Mo_2N and W_2N MXenes. The latter exhibited the lowest dissociation energy barrier of 0.28 eV and was therefore used in a microkinetic model at a maximum of 1075 K. It was shown that the reaction order increases with temperature. The third successive hydrogenation (NH_3 formation) was the rate-limiting step. The authors also investigated the situation where the N atoms from N_2 dissociation poisoned the surface. The surface coverage, ammonia production and back reactions were calculated.

Nakao et al.[161] studied NRR over Ru/Ca_2NH (100) within at the PBE level and confirmed the catalyst structure with AIMD simulations at 673 K. N_2 adsorption, formation of NH_x intermediates and hydrogen migration from Ru to $Ru/Ca_2NH_{1-x}e_x^-$ were incorporated in the microkinetic model as activation barriers and vibrational frequencies. The turnover frequency was calculated for each elementary step, considering the edge sites of Ru in Ru/Ca_2NH as active sites. The formation of the ammonia molecule from NH_2 and H_2 had the lowest TOF as the rate-determining step. The TOF values and the calculated activation energy of 0.61 eV agreed with the experimentally measured values. Furthemore, the coverage of N and H was also calculated at various temperature ($300-400\,°C$) and a pressure of 0.1 MPa.

Thermocatalytic ammonia synthesis over Fe (111) was studied with first-principles calculations coupled with kinetic Monte Carlo.[162] For all elementary reaction steps, reaction barriers were obtained at the PBE–D3 level with the transition state theory and cast into a kMC model. Kinetic simulations at 673 K and 20 atm and at 723 K and 200 atm (typical Haber-Bosch conditions). The former yielded a turn-over frequency of 17.7 s^{-1} on a 2x2 Fe (111) site in the steady state, which was compared with the experimentally determined TOF of 9.7 s^{-1}.

Fe-based catalysts was also studied by Liu et al.,[163] who performed microkinetic analysis on Fe_3 clusters, Fe_3/θ-Al_2O_3 (010), and Ru clusters at 1-100 bar and at temperatures of 300–1000 K. Upon confirming the associative mechanism, nitrogen adsorption was found to exhibit a linear BEP relation with the transition state energies on the metal surface. Furthermore, the calculated TOF for NRR over Fe_3/θ-Al_2O_3 (010) was comparable to that on the Ru catalyst (Ru B5 site), indicating that Fe cluster loading on Al_2O_3 (010) shows favorable performance for thermocatalytic NRR.

Another theoretical study of thermocatalytic NRR, encompassing first principles calculations using the B2LYP functional and kinetic modeling, was done by Ghoshal et al.,[164] who proposed the distal, alternating and enzymatic mechanisms for the side-on N_2 adsorption and a further reduction with H_2O over TiO_2 doped-Ru_n (n=5,6) clusters. The electron transfer from Ru to N_2 was confirmed by Bader charge analysis. The distal mechanism was found to be most feasible with the second hydrogenation as the rate-determining step. In addition, the authors investigated water oxidation and proposed a hydrogen molecule as a co-reactant to provide free cluster oxides after water oxidation. The calculated rate constants showed that doping Ru clusters with TiO_2 accelerates the kinetics compared to pristine Ru clusters.

5.2. Experimental-Data Based Modeling

Kinetic modelling can also be performed without first-principles input, as shown by Dahl et al.[165] who studied a Ru-based catalyst (single ruthenium crystal and $Ru/MgAl_2O_4$). Using experimental data from a continuously stirred tank reactor, a microkinetic model consisting of elementary reaction steps following the dissociative nitrogen mechanism and hydrogen dissociation was constructed. Calculating the number of active sites and the catalyst coverages, the model was able to capture the experimental data. Nitrogen dissociation was found to be a rate-determining step.

6. Reactor-Scale Modelling

Computational fluid dynamics (CFD) models are used to describe the macroscopic observables in a reactor, such as pressure fields, velocity regime etc. When coupled with kinetic modelling, it can provide reliable information about the performance of a reactor. However, CFD simulations of thermocatalytic nitrogen reduction are rare to the best of our knowledge no CFD calculations of photocatalytic NRR systems could be found. On the other hand, other reactions are being studied thermochemically or under light utilization using kinetics coupled with CFD or just CFD simulations: CO_2 reduction,[166–171] thermocatalytic ammonia synthesis and deposition,[172] or ammonia synthesis from urea instead of nitrogen.[173,174]

Industrial synthesis of ammonia was modeled by Mirvakili et al.[175] using computational fluid dynamics coupled with kinetic model. Building a two-dimensional mathematical model and solving partial differential equations for mass, heat transfer and momentum, CFD simulations were performed in a three-

ChemSusChem

Review

doi.org/10.1002/cssc.202301730

Chemistry Europe
European Chemical
Societies Publishing

bed reactor with a turbulent flow. Studying the impact of the feed temperature and the flow rate on the ammonia production, it was shown that the production deceased by 14% when the feed temperature is reduced by 40 °C, and decreased by 13% when the flow rate is reduced by 20%. Another study of ammonia synthesis was conducted by Nikzad *et al.*,[176] who examined the effects of three configurations of feed input in sperical radial flow and tubular reactors. The authors found that nitrogen conversion is higher in the spherical reactor (Config 4F), with a notably lower pressure drop, consistent with scale-up flow and higher nitrogen conversion compared to tubular reactor. In addition, they accompanied the output temperature of intermediate coolers, which showed that the lower input temperature of the second and third reactors leads to extremely increased nitrogen conversion rates (350%).

While kinetic and reactor-level modeling is scarce for photocatalytic nitrogen fixation, no successful attempts of building an overarching multiscale model exist. In contrast to photocatalytic NRR, meso- and macroscale simulations are somewhat more common for thermocatalytic ammonia synthesis. While coupling DFT with microkinetic models is relatively widely performed,[159–161,163–165,172] coupling DFT with kMC is rare, while higher-level integration (kMC or microkinetics and CFD) remains unexplored.

7. Conclusions

Photocatalytic nitrogen fixation has recently received considerable attention as a more sustainable and environmentally friendlier alternative to the conventional Haber-Bosch process, which is plagued by high energy consumption and carbon footprint due to the hydrogen required stemming from methane steam reforming.[4] Light-induced ammonia synthesis has been experimentally explored at the laboratory level, but theoretical studies have struggled to keep up. Theoretical studies of nitrogen photofixation at different modeling levels would effectively encapsulate atomistic-level calculations, kinetics, and macro-scale simulations.[27] Recently, an increasing number of theoretical studies appeared, which go hand in hand with the increasing computational power. However, there is still more to be done to move beyond solely atomistic studies.

Density functional theory (DFT) calculations remain the most widely used approach in computational materials science. They are still predominantly carried out at the GGA level with PBE or, less often PW91, functionals, but hybrid approaches (PBE0, HSE06) are being employed when more precise electronic structure is required. More commonly, however, Hubbard-U corrections (DFT+U) to account for strong Coulomb interactions and Grimme's corrections (D2 and D3) for dispersion interactions are applied instead.

TiO$_2$, g-C$_3$N$_4$, sulfides and bismuth oxyhalides are reported to be the most promising photocatalysts. Modifications of the catalysts with a favorable effect on their nitrogen fixation ability, such as dopants, cocatalysts, introduced defects (oxygen and nitrogen vacancies) and heterojunctions, which tend to decrease the band gap width, prevent electron-hole recombina-

tion, thus improve charge separation, and increase ammonia production yields and rates, have been abundantly studies. However, doping and vacancy formation can introduce new defect levels in the middle of the band gap, which act as recombination centers, resulting in less charge carrier recombination.[1] With first-principles approaches, band structure (valence band maximum, conduction band minimum), band gap energy, density of states and projected density of states are usually calculated.

The electronic properties of semiconductor photocatalysts are a good springboard for considering nitrogen adsorption at the active sites of the photocatalyst. Active sites are commonly introduced as defects that facilitate nitrogen adsorption, which can occur in the end-on or side-on configuration, followed by a proton-electron coupled (PEC) process, resulting in N$_2$ activation and elongation of the triple bond.[4] The calculations of adsorption energies, Bader or Hirshfeld charge analysis, and electron density difference are usually performed on these structures. Different adsorption regimes are possible, ranging from tentative physisorption to strong chemisorption. It has been well established that reactants, intermediates or products should not bind too strongly to the catalyst surface to avoid catalyst poisoning.[48,139]

Based on the adsorption configurations, different reaction mechanisms are possible. While the dissociative and associative mechanisms are theoretically possible on heterogeneous catalysts, most photocatalytic studies omit the dissociative pathway based on the calculated Gibbs free energies or adsorption modes. Cleaving a strong triple bond before the first hydrogenation requires a high energy input, which is not feasible in photocatalytic reactions. Instead of the dissociative, three associative pathways are commonly described in photocatalytic NRR: distal, alternating and enzymatic.[4] Among all three, the distal and alternating pathways are most commonly observed. Different reaction mechanisms are suggested based on the experimentally determined intermediates and products or, more frequently, based on DFT calculations. It has been shown that the end-on adsorption boosts the distal or alternating mechanism, while, the side-on configuration favours the enzymatic pathway. Most DFT studies are performed to complement photocatalytic experimental work, which generally uses water as a proton source, while DFT studies usually consider hydrogen as a proton source. While ammonia, hydrazine and nitrate (NO$_3^-$) are usually detected experimentally, however, DFT calculations focus on ammonia and occasionally on hydrazine as a side product.

Occassionally, *ab initio* Molecular Dynamics (AIMD) is used to confirm the thermodynamic stability of the photocatalyst model.[46–49] It is carried out at a chosen constant temperature (between 400 and 800 K), which is regulated by a thermostat (Nosé-Hoover). Simulations are performed in vacuum or water, when water is considered a proton source and its effect on the stability must be established. Moreover, time-dependent *ab initio* nonadiabatic molecular dynamic simulations can be used to model a charge-carrier recombination lifetime.[65,83]

Higher level simulations are far and few between. Meso- and macroscale simulations (microkinetic or kinetic Monte Carlo

ChemSusChem

Review

doi.org/10.1002/cssc.202301730

Chemistry
Europe
European Chemical
Societies Publishing

modeling, computational fluid dynamics) remain an uncharted territory. Most commonly, first principles computations are coupled with microkinetic modelling[160,161,163–165,172] and much rarely with kinetic Monte Carlo (,[162] considering ammonia synthesis only under thermocatalytic conditions. Few attempts at reactor modeling at the macro level were identified.[172]

Hence, this review primarily includes first-principles studies. However, it should be emphasized that DFT studies have predominantly focused on the ground state, neglecting the excited-state properties that are crucial for capturing the essence of the photocatalytic reactions. Very rarely, electron excitations have been modeled with TD-DFT but limited to static properties and no reaction mechanism data. Only nitrogen dissociation in the excited state has been modelled on Fe and Ru.[150,151]

Multiscale modeling of photocatalytic nitrogen fixation is still in its infancy although individual methods have been developed. Coupling atomistic simulations with meso- (kinetics) and macro-level (reactor modeling) simulations remains elusive although it has been achieved for other reactions, such as CO_2 hydrogenation. The nascent field has a great potential for computationally supported catalyst discovery and development, and process optimization, which could be afforded by multiscale models. Including the excited states in the atomistic simulations and an efficient coupling of scales remain prerequisites for that.

Acknowledgements

Conflict of Interests

The authors declare no conflict of interest.

Keywords: photocatalysis · nitrogen photofixation · ammonia synthesis · density functional theory · multiscale modelling

[1] R. Shi, Y. Zhao, G. I. N. Waterhouse, S. Zhang, T. Zhang, *ACS Catal.* **2019**, *9*, 9739.
[2] N. Gruber, J. N. Galloway, *Nature* **2008**, *451*, 293.
[3] M. Li, H. Huang, J. Low, C. Gao, R. Long, Y. Xiong, *Small Methods* **2018**, *3*, 1800388.
[4] K. Ithisuphalap, H. Zhang, L. Guo, Q. Yang, H. Yang, G. Wu, *Small Methods* **2018**, *3*, 1800352.
[5] C. Smith, A. K. Hill, L. Torrente-Murciano, *Energy Environ. Sci.* **2020**, *13*, 331.
[6] N. Tian, B. M. Comer, A. J. Medford, *ChemSusChem* **2023**.
[7] V. Kyriakou, I. Garagounis, A. Vourros, E. Vasileiou, M. Stoukides, *Joule* **2020**, *4*, 142.
[8] S. Wu, Z. Chen, K. Liu, W. Yue, L. Wang, J. Zhang, *ChemSusChem* **2020**, *13*, 3455.
[9] C. He, X. Li, D. Qiu, Y. Chen, Y. Lu, X. Cui, *Appl. Surf. Sci.* **2021**, *556*, 149753.
[10] H. Li, C. Mao, H. Shang, Z. Yang, Z. Ai, L. Zhang, *Nanoscale* **2018**, *10*, 15429.
[11] N. Bion, D. Duprez, F. Epron, *ChemSusChem* **2011**, *5*, 76.
[12] R. Li, *Chin. J. Catal.* **2018**, *39*, 1180.
[13] G. N. Schrauzer, T. D. Guth, *J. Am. Chem. Soc.* **1977**, *99*, 7189.
[14] Z. Wang, Y. Liu, B. Huang, Y. Dai, Z. Lou, G. Wang, X. Zhang, X. Qin, *Phys. Chem. Chem. Phys.* **2014**, *16*, 2758.
[15] S. Chen, D. Liu, T. Peng, *Solar RRL* **2020**, *5*, 2000487.
[16] Y. Wan, J. Xu, R. Lv, *Mater. Today* **2019**, *27*, 69.
[17] J. Chen, H. Cheng, L.-X. Ding, H. Wang, *Mater. Chem. Front.* **2021**, *5*, 5954.
[18] L. M. Azofra, *Curr. Opin. Electrochem.* **2022**, *35*, 101073.
[19] W. S. Koe, J. W. Lee, W. C. Chong, Y. L. Pang, L. C. Sim, *Environ. Sci. Pollut. Res. Int.* **2019**, *27*, 2522.
[20] L. Ran, J. Hou, S. Cao, Z. Li, Y. Zhang, Y. Wu, B. Zhang, P. Zhai, L. Sun, *Solar RRL* **2020**, *4*.
[21] Y. Huang, Y. Yu, Y. Yu, B. Zhang, *Solar RRL* **2020**, *4*.
[22] J. Yuan, X. Yi, Y. Tang, M. Liu, C. Liu, *Adv. Funct. Mater.* **2019**, *30*, 1906983.
[23] J. Low, J. Yu, M. Jaroniec, S. Wageh, A. A. Al-Ghamdi, *Adv. Mater.* **2017**, *29*, 1601694.
[24] H. Lee, J.-H. Lee, Y. Lee, E.-B. Cho, Y. J. Jang, *Appl. Surf. Sci.* **2023**, *620*, 156812.
[25] J. Hafner, C. Wolverton, G. Ceder, *MRS Bull.* **2006**, *31*, 659.
[26] P. J. Hasnip, K. Refson, M. I. J. Probert, J. R. Yates, S. J. Clark, C. J. Pickard, *Philos. Trans. R. Soc. London Ser. A* **2014**, *372*, 20130270.
[27] T. Karakasidis, C. Charitidis, *Mater. Sci. Eng. C* **2007**, *27*, 1082.
[28] R. Iftimie, P. Minary, M. E. Tuckerman, *Proc. Nat. Acad. Sci.* **2005**, *102*, 6654.
[29] M. Huš, M. Grilc, A. Pavlišič, B. Likozar, A. Hellman, *Catal. Today* **2019**, *338*, 128.
[30] P. Hohenberg, W. Kohn, *Phys. Rev.* **1964**, *136*, B864.
[31] X. Meng, N. Yun, Z. Zhang, *Can. J. Chem. Eng.* **2019**, *97*, 1982.
[32] N. Argaman, G. Makovn, *Am. J. Phys.* **2000**, *68*, 69.
[33] W. Kohn, L. J. Sham, *Phys. Rev.* **1965**, *140*, A1133.
[34] J. L. Bao, L. Gagliardi, D. G. Truhlar, *J. Phys. Chem. Lett.* **2018**, *9*, 2353.
[35] J. Tao, J. P. Perdew, V. N. Staroverov, G. E. Scuseria, *Phys. Rev. Lett.* **2003**, *91*, 146401.
[36] P. Mori-Sánchez, A. J. Cohen, *Phys. Chem. Chem. Phys.* **2014**, *16*, 14378.
[37] R. I. Eglitis, R. Jia, *Materials* **2023**, *16*, 7623.
[38] R. Eglitis, A. Popov, *J. Saudi Chem. Soc.* **2018**, *22*, 459.
[39] J. Enkovaara, C. Rostgaard, J. J. Mortensen, J. Chen, M. Dułak, L. Ferrighi, J. Gavnholt, C. Glinsvad, V. Haikola, H. A. Hansen, H. H. Kristoffersen, M. Kuisma, A. H. Larsen, L. Lehtovaara, M. Ljungberg, O. Lopez-Acevedo, P. G. Moses, J. Ojanen, T. Olsen, V. Petzold, N. A. Romero, J. Stausholm-Møller, M. Strange, G. A. Tritsaris, M. Vanin, M. Walter, B. Hammer, H. Häkkinen, G. K. H. Madsen, R. M. Nieminen, J. K. Nørskov, M. Puska, T. T. Rantala, J. Schiøtz, K. S. Thygesen, K. W. Jacobsen, *J. Phys. Condens. Matter* **2010**, *22*, 253202.
[40] C. Adamo, D. Jacquemin, *Chem. Soc. Rev.* **2013**, *42*, 845.
[41] J. Gavnholt, T. Olsen, M. Engelund, J. Schiøtz, *Phys. Rev. B* **2008**, *78*, 075441.
[42] A. P. Demchenko, V. I. Tomin, P.-T. Chou, *Chem. Rev.* **2017**, *117*, 13353.
[43] A. T. B. Gilbert, N. A. Besley, P. M. W. Gill, *J. Phys. Chem. A* **2008**, *112*, 13164.
[44] G. Levi, A. V. Ivanov, H. Jónsson, *Faraday Discuss.* **2020**, *224*, 448.
[45] A. V. Ivanov, G. Levi, E. Ö. Jónsson, H. Jónsson, *J. Chem. Theory Comput.* **2021**, *17*, 5034.
[46] S. Cao, B. Fan, Y. Feng, H. Chen, F. Jiang, X. Wang, *Chem. Eng. J.* **2018**, *353*, 147.
[47] J. Li, P. Liu, Y. Tang, H. Huang, H. Cui, D. Mei, C. Zhong, *ACS Catal.* **2020**, *10*, 2431.
[48] S. Wang, L. Shi, X. Bai, Q. Li, C. Ling, J. Wang, *ACS Cent. Sci.* **2020**, *6*, 1762.
[49] L. M. Azofra, C. Sun, L. Cavallo, D. R. MacFarlane, *Chem. Eur. J.* **2017**, *23*, 8275.
[50] H. Prats, F. Illas, R. Sayós, *Int. J. Quantum Chem.* **2017**, *118*, e25518.
[51] D. Drikakis, M. Frank, G. Tabor, *Energies* **2019**, *12*, 3272.
[52] Y. Boyjoo, M. Ang, V. Pareek, *Chem. Eng. Sci.* **2013**, *101*, 764.
[53] Y. Zhao, Y. Zhao, R. Shi, B. Wang, G. I. N. Waterhouse, L.-Z. Wu, C.-H. Tung, T. Zhang, *Adv. Mater.* **2019**, *31*, 1806482.
[54] Y. Zhang, X. Chen, S. Zhang, L. Yin, Y. Yang, *Chem. Eng. J.* **2020**, *401*, 126033.

[55] J. Li, D. Wang, R. Guan, Y. Zhang, Z. Zhao, H. Zhai, Z. Sun, *ACS Sustainable Chem. Eng.* **2020**, *8*, 18258.

[56] S. Wu, Z. Chen, W. Yue, S. Mine, T. Toyao, M. Matsuoka, X. Xi, L. Wang, J. Zhang, *ACS Catal.* **2021**, *11*, 4362.

[57] T. Žibert, B. Likozar, M. Huš, *Fuel* **2023**, *334*, 126451.

[58] W. Ye, M. Arif, X. Fang, M. A. Mushtaq, X. Chen, D. Yan, *ACS Appl. Mater. Interfaces* **2019**, *11*, 28809.

[59] C. Ren, Y. Zhang, Y. Li, Y. Zhang, S. Huang, W. Lin, K. Ding, *J. Phys. Chem. C* **2019**, *123*, 17296.

[60] D. Yang, X. Cai, J. Zhang, B. Ding, Y. Zhao, X. Gu, L. Mao, Y. Qiang, *J. Alloys* **2021**, *869*, 158809.

[61] S. Hu, X. Chen, Q. Li, F. Li, Z. Fan, H. Wang, Y. Wang, B. Zheng, G. Wu, *Appl. Catal. B* **2017**, *201*, 58.

[62] S. Hu, X. Qu, J. Bai, P. Li, Q. Li, F. Wang, L. Song, *ACS Sustainable Chem. Eng.* **2017**, *5*, 6863.

[63] K. Wang, G. Gu, S. Hu, J. Zhang, X. Sun, F. Wang, P. Li, Y. Zhao, Z. Fan, X. Zou, *Chem. Eng. J.* **2019**, *368*, 896.

[64] G. Liu, Z. Tang, X. Gu, N. Li, H. Lv, Y. Huang, Y. Zeng, Q. Meng, Y. Zhou, C. Wang, *Appl. Catal. B* **2022**, *317*, 121752.

[65] Y. Zhao, S. Zhou, J. Zhao, Y. Du, S. X. Dou, *J. Phys. Chem. Lett.* **2020**, *11*, 9304.

[66] X. Chen, X. Zhang, Y.-H. Li, M.-Y. Qi, J.-Y. Li, Z.-R. Tang, Z. Zhou, Y.-J. Xu, *Appl. Catal. B* **2021**, *281*, 119516.

[67] J. Di, J. Xia, M. F. Chisholm, J. Zhong, C. Chen, X. Cao, F. Dong, Z. Chi, H. Chen, Y.-X. Weng, J. Xiong, S.-Z. Yang, H. Li, Z. Liu, S. Dai, *Adv. Mater.* **2019**, *31*, 1807576.

[68] Xing'an Dong, Z. Cui, X. Shi, P. Yan, Z. Wang, A. C. Co, F. Dong, *Angew. Chem. Int. Ed.* **2022**, *61*, e2022009.

[69] Y. Li, X. Chen, M. Zhang, Y. Zhu, W. Ren, Z. Mei, M. Gu, F. Pan, *Catal. Sci. Technol.* **2019**, *9*, 803.

[70] H. Yin, Z. Chen, Y. Peng, S. Xiong, Y. Li, H. Yamashita, J. Li, *Angew. Chem. Int. Ed.* **2022**, *61*, e2021142.

[71] X. Hui, L. Li, Q. Xia, S. Hong, L. Hao, A. W. Robertson, Z. Sun, *Chem. Eng. J.* **2022**, *438*, 135485.

[72] G. Dong, X. Huang, Y. Bi, *Angew. Chem. Int. Ed.* **2022**, *61*, e2022042.

[73] X. Liu, Y. Luo, C. Ling, Y. Shi, G. Zhan, H. Li, H. Gu, K. Wei, F. Guo, Z. Ai, L. Zhang, *Appl. Catal. B* **2022**, *301*, 120766.

[74] G. Zhang, X. Yuan, B. Xie, Y. Meng, Z. Ni, S. Xia, *Chem. Eng. J.* **2022**, *433*, 133670.

[75] Y. Zhao, Y. Zhao, G. l. N. Waterhouse, L. Zheng, X. Cao, F. Teng, L.-Z. Wu, C.-H. Tung, D. O'Hare, T. Zhang, *Adv. Mater.* **2017**, *29*, 1703828.

[76] Y. Zhao, L. Zheng, R. Shi, S. Zhang, X. Bian, F. Wu, X. Cao, G. l. N. Waterhouse, T. Zhang, *Adv. Energy Mater.* **2020**, *10*, 2002199.

[77] C. Zhang, Y. Xu, C. Lv, X. Zhou, Y. Wang, W. Xing, Q. Meng, Y. Kong, G. Chen, *ACS Appl. Mater. Interfaces* **2019**, *11*, 29917.

[78] K.-Q. Hu, P.-X. Qiu, L.-W. Zeng, S.-X. Hun, L. Mei, S.-W. An, Z.-W. Huang, X.-H. Kong, J.-H. Lan, J.-P. Yu, Z.-H. Zhang, Z.-F. Xu, J. K. Gibson, Z.-F. Chai, Y.-F. Bu, W.-Q. Shi, *Angew. Chem. Int. Ed.* **2020**, *59*, 20666.

[79] H. Han, Y. Yang, J. Liu, X. Zheng, X. Wang, S. Meng, S. Zhang, X. Fu, S. Chen, *ACS Appl. Energ. Mater.* **2020**, *3*, 11275.

[80] X. Xue, H. Chen, Y. Xiong, R. Chen, M. Jiang, G. Fu, Z. Xi, X. L. Zhang, J. Ma, W. Fang, Z. Jin, *ACS Appl. Mater. Interfaces* **2021**, *13*, 4975.

[81] Y. Sun, W. Pei, M. Xie, S. Xu, S. Zhou, J. Zhao, K. Xiao, Y. Zhu, *Chem. Sci.* **2020**, *11*, 2440.

[82] X. Li, H. Shi, S. Zuo, B. Gao, C. Han, T. Wang, C. Yao, C. Ni, *Chem. Eng. J.* **2021**, *414*, 128797.

[83] W. Pei, S. Zhou, J. Zhao, Y. Du, S. X. Dou, *J. Mater. Chem. A* **2020**, *8*, 20570.

[84] X. Lv, W. Wei, F. Li, B. Huang, Y. Dai, *Nano Lett.* **2019**, *19*, 6391.

[85] K. Bhattacharyya, A. Datta, *Phys. Chem. Chem. Phys.* **2019**, *21*, 12346.

[86] H. Liu, Z. Fang, Y. Su, Y. Suo, S. Huang, Y. Zhang, K. Ding, *Chem. Asian J.* **2018**, *13*, 799.

[87] A. J. Medford, A. Vojvodic, J. S. Hummelshøj, J. Voss, F. Abild-Pedersen, F. Studt, T. Bligaard, A. Nilsson, J. K. Nørskov, *J. Catal.* **2015**, *328*, 36.

[88] T. Bligaard, J. Nørskov, S. Dahl, J. Matthiesen, C. Christensen, J. Sehested, *J. Catal.* **2004**, *224*, 206.

[89] C. J. H. Jacobsen, S. Dahl, B. S. Clausen, S. Bahn, A. Logadottir, J. K. Nørskov, *J. Am. Chem. Soc.* **2001**, *123*, 8404.

[90] X.-Y. Xie, P. Xiao, W.-H. Fang, G. Cui, W. Thiel, *ACS Catal.* **2019**, *9*, 9178.

[91] J. Yang, Y. Guo, R. Jiang, F. Qin, H. Zhang, W. Lu, J. Wang, J. C. Yu, *J. Am. Chem. Soc.* **2018**, *140*, 8497.

[92] G. Zhang, X. Yang, C. He, P. Zhang, H. Mi, *J. Mater. Chem. A* **2020**, *8*, 334.

[93] T. Hou, Q. Li, Y. Zhang, W. Zhu, K. Yu, S. Wang, Q. Xu, S. Liang, L. Wang, *Appl. Catal. B* **2020**, *273*, 119072.

[94] R. Guan, D. Wang, Y. Zhang, C. Liu, W. Xu, J. Wang, Z. Zhao, M. Feng, Q. Shang, Z. Sun, *Appl. Catal. B* **2021**, *282*, 119580.

[95] W. Zhao, J. Zhang, X. Zhu, M. Zhang, J. Tang, M. Tan, Y. Wang, *Appl. Catal. B* **2014**, *144*, 468.

[96] W. Gao, X. Li, S. Luo, Z. Luo, X. Zhang, R. Huang, M. Luo, *J. Colloid Interface Sci.* **2021**, *585*, 20.

[97] B. M. Comer, Y.-H. Liu, M. B. Dixit, K. B. Hatzell, Y. Ye, E. J. Crumlin, M. C. Hatzell, A. J. Medford, *J. Am. Chem. Soc.* **2018**, *140*, 15157.

[98] Z. Zhao, D. Wang, R. Gao, G. Wen, M. Feng, G. Song, J. Zhu, D. Luo, H. Tan, X. Ge, W. Zhang, Y. Zhang, L. Zheng, H. Li, Z. Chen, *Angew. Chem. Int. Ed.* **2021**, *60*, 11910.

[99] H. Ma, Z. Shi, Q. Li, S. Li, *J. Phys. Chem. Solids* **2016**, *99*, 51.

[100] S. Li, X. Chen, S. Hu, Q. Li, J. Bai, F. Wang, *RSC Adv.* **2016**, *6*, 45931.

[101] G. Dong, W. Ho, C. Wang, *J. Mater. Chem. A* **2015**, *3*, 23435.

[102] A. Shi, H. Li, S. Yin, Z. Hou, J. Rong, J. Zhang, Y. Wang, *Appl. Catal. B* **2018**, *235*, 197.

[103] Z. Li, G. Gu, S. Hu, X. Zou, G. Wu, *Chin. J. Catal.* **2019**, *40*, 1178.

[104] H. Wang, Y. Bu, G. Wu, X. Zou, *Dalton Trans.* **2019**, *48*, 11724.

[105] C. Yao, R. Wang, Z. Wang, H. Lei, X. Dong, C. He, *J. Mater. Chem. A* **2019**, *7*, 27547.

[106] X.-W. Guo, S.-M. Chen, H.-J. Wang, Z.-M. Zhang, H. Lin, L. Song, T.-B. Lu, *J. Mater. Chem. A* **2019**, *7*, 19831.

[107] H. Liu, P. Wu, H. Li, Z. Chen, L. Wang, X. Zeng, Y. Zhu, Y. Jiang, X. Liao, B. S. Haynes, J. Ye, C. Stampfl, J. Huang, *Appl. Catal. B* **2019**, *259*, 118026.

[108] C. Liang, H.-Y. Niu, H. Guo, C.-G. Niu, D.-W. Huang, Y.-Y. Yang, H.-Y. Liu, B.-B. Shao, H.-P. Feng, *Chem. Eng. J.* **2020**, *396*, 125395.

[109] X. Yang, S. Zhou, S. Huang, J. Zhao, *J. Phys. Chem. C* **2020**, *124*, 23798.

[110] M. Liu, Y. Wang, X. Kong, L. Tan, L. Li, S. Cheng, G. Botton, H. Guo, Z. Mi, C.-J. Li, *iScience* **2019**, *17*, 208.

[111] D. Wu, R. Wang, C. Yang, Y. An, H. Lu, H. Wang, K. Cao, Z. Gao, W. Zhang, F. Xu, K. Jiang, *J. Colloid Interface Sci.* **2019**, *556*, 111.

[112] H. Li, J. Shang, J. Shi, K. Zhao, L. Zhang, *Nanoscale* **2016**, *8*, 1986.

[113] X. Xue, R. Chen, H. Chen, Y. Hu, Q. Ding, Z. Liu, L. Ma, G. Zhu, W. Zhang, Q. Yu, J. Liu, J. Ma, Z. Jin, *Nano Lett.* **2018**, *18*, 7372.

[114] H. Li, J. Shang, Z. Ai, L. Zhang, *J. Am. Chem. Soc.* **2015**, *137*, 6393.

[115] Y. Liu, Z. Hu, J. C. Yu, *Chem. Mater.* **2020**, *32*, 1488.

[116] P. Li, Z. Zhou, Q. Wang, M. Guo, S. Chen, J. Low, R. Long, W. Liu, P. Ding, Y. Wu, Y. Xiong, *J. Am. Chem. Soc.* **2020**, *142*, 12430.

[117] K. Gao, C. Zhang, Y. Zhang, X. Zhou, S. Gu, K. Zhang, X. Wang, X. Song, *J. Colloid Interface Sci.* **2022**, *614*, 12.

[118] X. Ren, M. Xia, B. Chong, X. Yan, B. Lin, G. Yang, *Chem. Eng. Sci.* **2022**, *257*, 117734.

[119] N. Zhang, A. Jalil, D. Wu, S. Chen, Y. Liu, C. Gao, W. Ye, Z. Qi, H. Ju, C. Wang, X. Wu, L. Song, J. Zhu, Y. Xiong, *J. Am. Chem. Soc.* **2018**, *140*, 9434.

[120] W. Zhao, H. Xi, M. Zhang, Y. Li, J. Chen, J. Zhang, X. Zhu, *Chem. Commun.* **2015**, *51*, 4785.

[121] Z. Li, Z. Pan, S. Cai, Z. Gao, Z. Li, R. Fu, Z. Zhao, X. Mu, L. Li, *ACS Sustainable Chem. Eng.* **2021**, *9*, 13630.

[122] S. Zhang, Y. Zhao, R. Shi, C. Zhou, G. l. N. Waterhouse, L.-Z. Wu, C.-H. Tung, T. Zhang, *Adv. Energy Mater.* **2020**, *10*, 1901973.

[123] G. Li, F. Li, J. Liu, C. Fan, *J. Solid State Chem.* **2020**, *285*, 121245.

[124] S. Shang, W. Xiong, C. Yang, B. Johannessen, R. Liu, H.-Y. Hsu, Q. Gu, M. K. H. Leung, J. Shang, *ACS Nano* **2021**, *15*, 9670.

[125] S. Hu, X. Chen, Q. Li, Y. Zhao, W. Mao, *Catal. Sci. Technol.* **2016**, *6*, 5884.

[126] J. Liu, M. S. Kelley, W. Wu, A. Banerjee, A. P. Douvalis, J. Wu, Y. Zhang, G. C. Schatz, M. G. Kanatzidis, *Proc. Nat. Acad. Sci.* **2016**, *113*, 5530.

[127] Z.-K. Shen, Y.-J. Yuan, P. Wang, W. Bai, L. Pei, S. Wu, Z.-T. Yu, Z. Zou, *ACS Appl. Mater. Interfaces* **2020**, *12*, 17343.

[128] X. Gao, L. An, D. Qu, W. Jiang, Y. Chai, S. Sun, X. Liu, Z. Sun, *Sci. Bull.* **2019**, *64*, 918.

[129] X. Ma, J. Hu, M. Zheng, D. Li, H. Lv, H. He, C. Huang, *Appl. Surf. Sci.* **2019**, *489*, 684.

[130] B. Hu, B.-H. Wang, Z. Jun Bai, L. Chen, J.-K. Guo, S. Shen, T.-L. Xie, C.-T. Au, L.-L. Jiang, S.-F. Yin, *Chem. Eng. J.* **2022**, *442*, 136211.

[131] T. Hou, H. Peng, Y. Xin, S. Wang, W. Zhu, L. Chen, Y. Yao, W. Zhang, S. Liang, L. Wang, *ACS Catal.* **2020**, *10*, 5502.

[132] J. Qin, X. Hu, X. Li, Z. Yin, B. Liu, K. Ho Lam, *Nano Energy* **2019**, *61*, 27.

[133] G. Li, W. Yang, S. Gao, Q. Shen, J. Xue, K. Chen, Q. Li, *Chem. Eng. J.* **2021**, *404*, 127115.

[134] C. Zhang, G. Chen, C. Lv, Y. Yao, Y. Xu, X. Jin, Q. Meng, *ACS Sustainable Chem. Eng.* **2018**, *6*, 11190.

[135] X. Sun, D. Jiang, L. Zhang, S. Sun, W. Wang, *ACS Sustainable Chem. Eng.* **2017**, *5*, 9965.

[136] H. Li, M. Xia, B. Chong, H. Xiao, B. Zhang, B. Lin, B. Yang, G. Yang, *ACS Catal.* **2022**, *12*, 10361.

[137] Y. Zhang, L. Ran, Y. Zhang, P. Zhai, Y. Wu, J. Gao, Z. Li, B. Zhang, C. Wang, Z. Fan, X. Zhang, J. Cao, D. Jin, L. Sun, J. Hou, *ACS Nano* **2021**, *15*, 17820.

[138] S. Yao, J. Liu, F. Liu, B. Wang, Y. Ding, L. Li, C. Liu, F. Huang, J. Fang, Z. Lin, M. Wang, *Environ. Sci.-Nano* **2022**, *9*, 1996.

[139] M. Králik, *Chem. Pap.* **2014**, *68*, 1625–1638.

[140] J. Qian, S. Zhao, W. Dang, Y. Liao, W. Zhang, H. Wang, L. Lv, L. Luo, H.-Y. Jiang, J. Tang, *Adv. Sustainable Syst.* **2021**, *5*, 2000282.

[141] Y. Liao, J. Qian, G. Xie, Q. Han, W. Dang, Y. Wang, L. Lv, S. Zhao, L. Luo, W. Zhang, H.-Y. Jiang, J. Tang, *Appl. Catal. B* **2020**, *273*, 119054.

[142] C. Li, T. Wang, Z.-J. Zhao, W. Yang, J.-F. Li, A. Li, Z. Yang, G. A. Ozin, J. Gong, *Angew. Chem. Int. Ed.* **2018**, *57*, 5278.

[143] H. Li, H. Zhao, C. Li, B. Li, B. Tao, S. Gu, G. Wang, H. Chang, *Appl. Surf. Sci.* **2022**, *600*, 154105.

[144] Z. Zhao, C. Choi, S. Hong, H. Shen, C. Yan, J. Masa, Y. Jung, J. Qiu, Z. Sun, *Nano Energy* **2020**, *78*, 105368.

[145] B. Liu, A. S. Yasin, T. Musho, J. Bright, H. Tang, L. Huang, N. Wu, *J. Electrochem. Soc.* **2019**, *166*, H3091.

[146] A. S. Yasin, B. Liu, N. Wu, T. Musho, *Comput. Mater. Sci.* **2019**, *158*, 65.

[147] G. Zhang, T. Dai, Y. Wang, Y. Meng, B. Xie, Z. Ni, S. Xia, *Appl. Catal. B* **2021**, *288*, 119990.

[148] B. Sun, Z. Liang, Y. Qian, X. Xu, Y. Han, J. Tian, *ACS Appl. Mater. Interfaces* **2020**, *12*, 7257.

[149] B. M. Comer, A. J. Medford, *ACS Sustainable Chem. Eng.* **2018**, *6*, 4648.

[150] J. M. P. Martirez, E. A. Carter, *J. Am. Chem. Soc.* **2017**, *139*, 4390.

[151] J. M. P. Martirez, E. A. Carter, *Sci. Adv.* **2017**, *3*, 1.

[152] J. M. P. Martirez, E. A. Carter, *ACS Nano* **2016**, *10*, 2940.

[153] R. Egeberg, S. Dahl, A. Logadottir, J. Larsen, J. Nørskov, I. Chorkendorff, *Surf. Sci.* **2001**, *491*, 183.

[154] H. Falsig, J. Shen, T. S. Khan, W. Guo, G. Jones, S. Dahl, T. Bligaard, *Top. Catal.* **2013**, *57*, 80.

[155] A. Vojvodic, A. J. Medford, F. Studt, F. Abild-Pedersen, T. S. Khan, T. Bligaard, J. Nørskov, *Chem. Phys. Lett.* **2014**, *598*, 108.

[156] M. Hammerschmidt, S. Döpking, S. Burger, S. Matera, *J. Phys. Chem. C* **2020**, *124*, 3177.

[157] W. C. Chueh, C. Falter, M. Abbott, D. Scipio, P. Furler, S. M. Haile, A. Steinfeld, *Science* **2010**, *330*, 1797.

[158] A. A. Khan, M. Tahir, *J. CO2 Util.* **2019**, *29*, 205.

[159] J. R. Christianson, D. Zhu, R. J. Hamers, J. R. Schmidt, *J. Phys. Chem. B* **2013**, *118*, 195.

[160] J. D. Gouveia, Á. Morales-García, F. Viñes, J. R. B. Gomes, F. Illas, *ACS Catal.* **2020**, *10*, 5049.

[161] T. Nakao, T. Tada, H. Hosono, *J. Phys. Chem. C* **2019**, *124*, 2070.

[162] J. Qian, Q. An, A. Fortunelli, R. J. Nielsen, W. A. Goddard, *J. Am. Chem. Soc.* **2018**, *140*, 6288.

[163] J.-C. Liu, X.-L. Ma, Y. Li, Y.-G. Wang, H. Xiao, J. Li, *Nat. Commun.* **2018**, *9*, 1.

[164] S. Ghoshal, A. Pramanik, P. Sarkar, *Phys. Chem. Chem. Phys.* **2021**, *23*, 1527.

[165] S. Dahl, J. Sehested, C. Jacobsen, E. Tornqvist, I. Chorkendorff, *J. Catal.* **2000**, *192*, 391.

[166] R. J. Braham, A. T. Harris, *Phys. Chem. Chem. Phys.* **2013**, *15*, 12373.

[167] F. Chu, S. Li, H. Chen, L. Yang, O. Ola, M. Maroto-Valer, X. Du, Y. Yang, *Energy Convers. Manage.* **2017**, *149*, 514.

[168] H. Zhang, J. D. Smith, *Sol. Energy* **2019**, *188*, 935.

[169] S. Bhatta, D. Nagassou, S. Mohsenian, J. Trelles, *Sol. Energy* **2019**, *178*, 201.

[170] C. Du, X. Wang, W. Chen, S. Feng, J. Wen, Y. Wu, *Mater. Today* **2020**, *6*, 100071.

[171] X. Lu, X. Luo, W. A. Thompson, J. Z. Y. Tan, M. M. Maroto-Valer, *Front. Chem. Sci. Eng.* **2021**, *16*, 1149.

[172] S. Deshmukh, A. Mhadeshwar, D. Vlachos, *ACS Div. Fuel Chem. Preprint Papers* **2003**, *48*, 936.

[173] J. Sahu, V. R. K. Chava, S. Hussain, A. Patwardhan, B. Meikap, *J. Ind. Eng. Chem.* **2010**, *16*, 577.

[174] J. N. Sahu, S. Hussain, B. C. Meikap, *Korean J. Chem. Eng.* **2011**, *28*, 1380.

[175] A. Mirvakili, Z. Eksiri, P. Biniaz, N. Mohaghegh, *J. Taiwan Inst. Chem. Eng.* **2021**, *121*, 1.

[176] A. Nikzad, D. Iranshahi, M. Ranjbaran, E. Bagherpour-Ardakani, *Fuel* **2022**, *321*, 123945.